Geophys. J. Int. (2008) **173,** 958–978 doi: 10.1111/j.1365-246X.2008.03774.x

A comparison of observed and simulated site response in the Rhône valley

D. Roten,[1,*] D. Fäh,[1] K. B. Olsen[2] and D. Giardini[1]

[1]*Institute of Geophysics, ETH Hönggerberg,* 8093 *Zürich, Switzerland. E-mail: droten@sciences.sdsu.edu*
[2]*Department of Geological Sciences, San Diego State University, San Diego, CA, USA*

Accepted 2008 February 27. Received 2008 February 26; in original form 2007 July 11

SUMMARY

Site effects in the city of Sion in the Rhône valley are analysed from weak motion signals recorded on a dense temporary array. We simulate the recorded events with a 3-D finite difference method for frequencies up to 4 Hz using a recently developed velocity model of the Sion basin.

Site-to-reference Fourier spectral ratios are computed from 16 local and regional events. All sites exhibit amplification factors of up to 12 between 0.5 and 0.6 Hz, which can be reproduced by the numerical simulations. By rotating the weak motion to directions parallel and perpendicular to the valley axis, we show that this low-frequency amplification is caused by the SH_{00} and SV_0 fundamental modes of 2-D resonance.

Additional peaks of amplification can be observed at higher frequencies, with amplification factors of up to 20 at some sites.

Application of the high-resolution frequency-wavenumber and the multiple signal characterization method to the vertical component of recorded and simulated signals show that edge-generated surface waves arriving from almost all directions dominate the wavefield at 1.25 and 2.50 Hz.

Peak ground velocities computed from the simulated ground motion show interference patterns that depend strongly on the incidence direction, and the computed amplification of peak ground velocities are generally in agreement with the observations.

We conclude that the complex 3-D geometry of the basin needs to be considered to evaluate site effects up to at least 2.5 Hz.

Key words: Earthquake ground motions; Site effects; Computational seismology.

1 INTRODUCTION

The impact of local ground motion amplification on earthquake damage was demonstrated during many recent damaging earthquakes. In some cases, the trapping of waves in horizontally layered media has been able to explain the observed ground motion and increased damage (e.g. Hough *et al.* 1990). If lateral heterogeneities are present, as in the case of 2-D or 3-D structures, this trapping will also affect surface waves. A common example of such 3-D structures are sedimentary basins filled with unconsolidated low-velocity deposits. Many numerical studies of seismic wave propagation in 2-D and 3-D basins have shown that basin edges play a major role in amplifying ground motion (e.g. Bard & Bouchon 1980a,b, 1985; Frankel & Vidale 1992; Olsen *et al.* 2006). There is also good observational evidence for basin-edge-generated surface waves and for basin-focusing effects on ground motions (Frankel *et al.* 2001; Joyner 2000). A well-known example includes the damage belts reported after the 1995 Kobe earthquake (Kawase 1996).

In the framework of the SHAKE-VAL project, we are studying earthquake site effects in the Rhône valley, which is located in the area of the highest seismicity in Switzerland. The Valais region was struck by several large earthquakes in the last centuries, for example, the 1946 *M* 6.1 earthquake of Sierre and the 1855 *M* 6.5 and 1755 *M* 6.1 earthquakes of Visp and Brig. Since the last large earthquake of 1946 the area has undergone extensive development, especially on the soft unconsolidated Rhône sediments, raising concern about the impact of site effects during future earthquakes.

Only a few studies on earthquake site effects in the Rhône valley have been published. Frischknecht *et al.* (2005) performed 2-D numerical simulations with the indirect boundary element method for a set of profiles below the city of Sion. They found that the largest amplification will occur at frequencies between 0.5 and 0.8 Hz due to the 2-D resonance of the deep basin; for the central valley they predicted amplification factors of up to 12. However, these findings have not yet been verified by earthquake observations because only

*Now at: Department of Geological Sciences, San Diego State University, San Diego, CA, USA.

a few high-quality earthquake records have been acquired on the unconsolidated deposits of the Rhône valley.

In this study, we analyse the site response of the Rhône valley from earthquake signals recorded on a dense temporary array of weak motion seismometers. We will quantify the average amplification by computing site-to-reference spectral ratios from a number of local and regional events.

To aid interpretation of our results, we simulated 3-D wave propagation in the Sion basin with the 3-D finite difference method. These simulations were conducted with a recent velocity model that has been developed for the central Valais area. Shear wave velocities in this model are based on results from ambient noise array measurements. We model four of the recorded events and compare synthetic site-to-reference spectral ratios with the observations to assess the reliability of the newly developed velocity model. We apply a frequency-wavenumber method to the synthetic and observed earthquake signals to estimate the direction of origin of seismic waves at the peak frequencies of amplification.

Additionally we perform a simulation of the 1946 M 6.1 Sierre main shock to estimate the importance of site effects during this historical earthquake. Finally we compute peak ground velocities from all simulations to analyse the interference patterns and identify the effects generating the peak amplifications.

2 GEOPHYSICAL SETTING

The Rhône valley is a deeply eroded glacial valley filled with unconsolidated Quaternary deposits (Fig. 1). The structure of the sediment–bedrock interface is constrained from seismic reflection profiles (Pfiffner *et al.* 1997; Besson *et al.* 1993) and from gravimetric studies (e.g. Rosselli 2001). The thickness of the sedimentary fill reaches up to 1000 m at some places; below the city of Sion, the basin is about 500 m deep and less than 2000 m wide.

To assess site effects in the Rhône valley with numerical simulations, an accurate geophysical model of the site is required. Because a leading cause of amplification is the trapping of S- and surface waves in the sediments, the shear wave velocity is the most important parameter in the geophysical model. To improve the estimates of shear wave velocities in the unconsolidated deposits, a series of ambient noise array measurements was carried out at different sites in the Rhône valley. Fig. 2 shows examples of shear wave velocities obtained from ambient noise recorded at four representative sites.

Circular array layouts with apertures of up to 800 m were used to estimate apparent Rayleigh wave phase velocities with the high-resolution frequency-wavenumber method (Capon 1969; Kind *et al.* 2005). However, dispersion curves alone cannot be used to estimate shear wave velocities in the deeper part of the basin because standing waves evoked by 2-D resonance dominate at low frequencies (Roten *et al.* 2006). This violates a basic supposition of the method that requires that horizontally propagating surface waves dominate the noise wavefield.

Analysis of noise recorded on linear arrays running perpendicular to the valley axis allows definition of the different mode 2-D resonance frequencies. Together with the dispersion curves obtained from circular arrays, these 2-D resonance frequencies are inverted for the shear wave velocities of the unconsolidated deposits (Roten & Fäh 2007). For this method, the forward problem of computing the 2-D resonance frequencies is solved by Rayleigh's principle with a method proposed by Paolucci (1999). The combined inversion improves the resolution in the lower part of the sedimentary fill, and

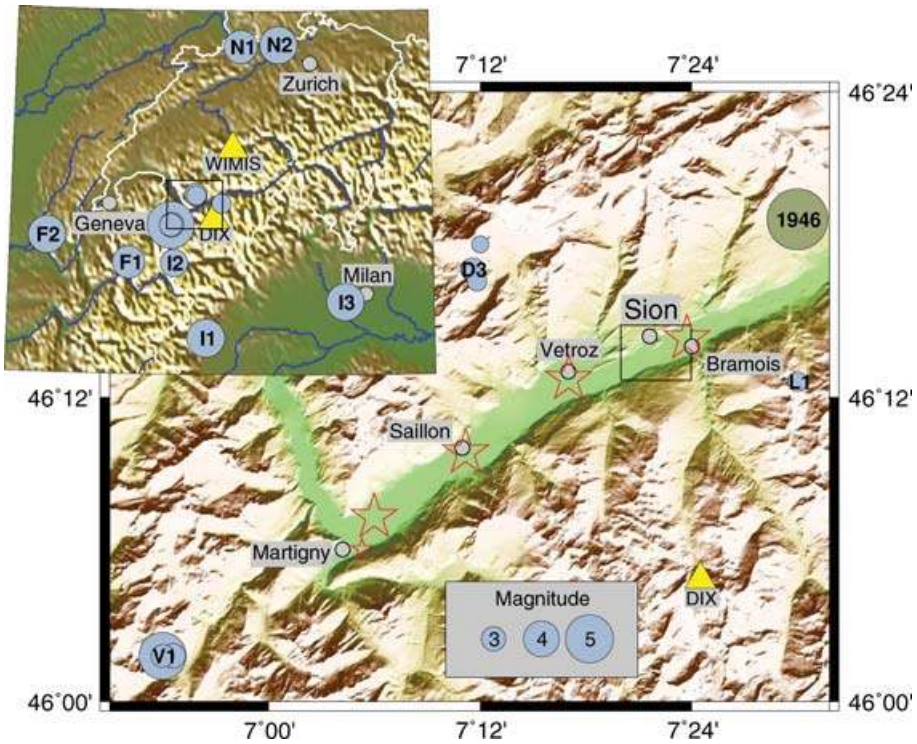

Figure 1. Map of the Rhône valley. Red stars show locations of ambient noise array measurements, yellow triangles the position of the broad-band stations WIMIS and DIX. Epicentres of recorded earthquakes are plotted with blue circles; the green circle shows the epicentre of the 1946 Sierre earthquake. Reproduced by permission of Swisstopo (BA081013).

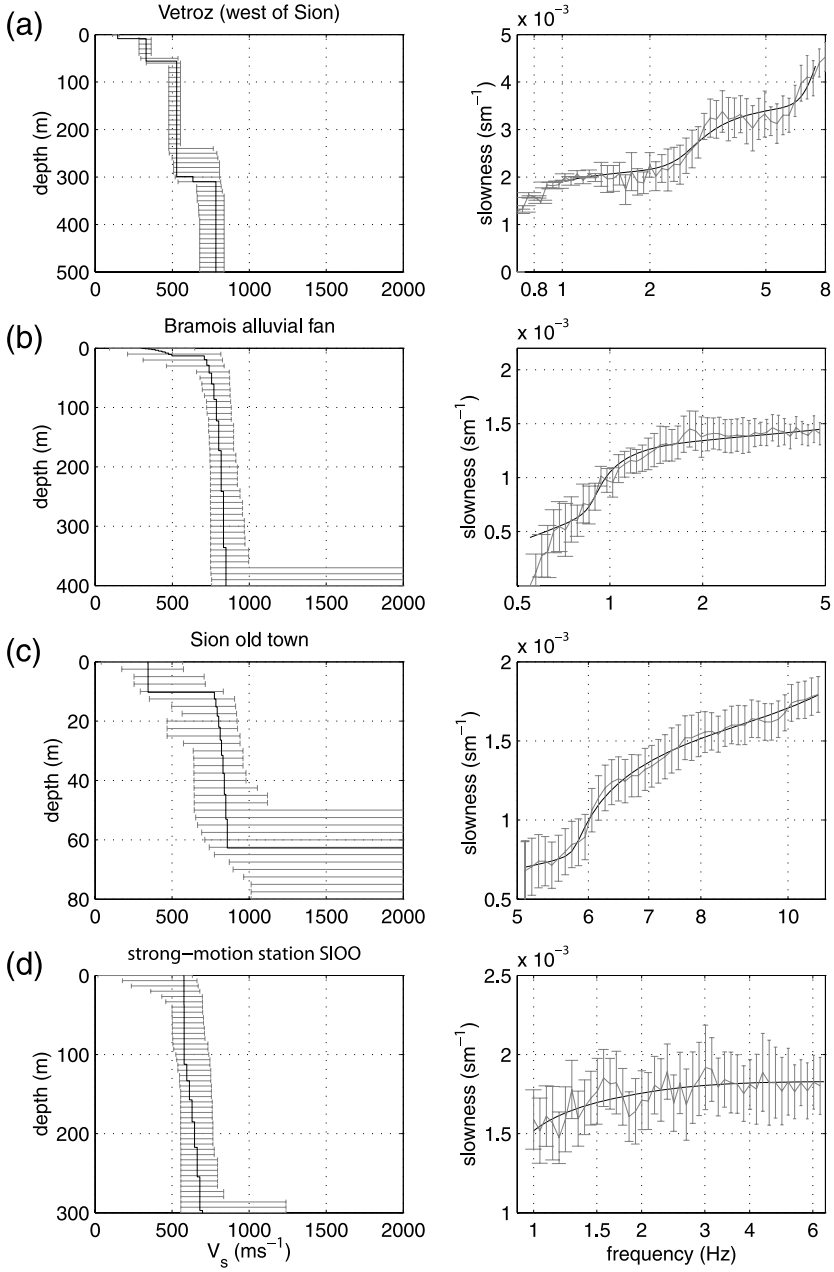

Figure 2. Inversion results obtained from array measurements of ambient noise in the Sion region. *Right-hand side* measured dispersion curves with standard deviations (grey) and dispersion curves for the best-fitting velocity model (black). *Left-hand side* Shear wave velocities obtained from inversion. Errorbars are showing the velocity range contained in models that yield dispersion curves within the standard deviation.

it has successfully been tested on a synthetic ambient noise data set (Roten & Fäh 2007). Such combined inversions were performed at three sites west of Sion, near the towns of Vétroz, Saillon and Martigny (Fig. 1). The depth to the bedrock cannot be resolved from ambient noise array measurements. Instead, the depth reported from gravimetry or reflection seismics needs to be introduced as a priory information in the combined inversion of shear wave velocities (Roten & Fäh 2007).

Additionally, circular arrays were recorded on the Bramois alluvial fan, in the old town of Sion and in the vicinity of the three permanent strong-motion stations SIOV, SIOO and SIOM (Fig. 3). We used the 'geopsy' (available at http://www.geopsy.org) program package (Wathelet *et al.* 2004) for frequency-wavenumber analysis and for inversion of dispersion curves.

On the basis of array measurements performed at different parts of the Rhône sediments, the analysed sites can roughly be subdivided into two categories:

(i) *Fine lacustrine and deltaic deposits* (Martigny, Saillon and Vétroz, Fig. 2a): At these sites a very shallow low-velocity layer (less than 15 m deep) with shear wave velocities as low as 100 m s^{-1} was resolved. Below this layer, V_s ranges between 320 and 500 m s^{-1} until about 250 m depth, where a strong velocity contrast occurs, and V_s increases to 650–800 m s^{-1}. Shear wave velocities in the lowest part of the sediment are in the range between 700 and 1000 m s^{-1} (refer to Roten & Fäh 2007, for detailed results).

(ii) *alluvial fans* (old town of Sion, Bramois, Figs 2b and c): Apart from a shallow low-velocity layer, shear wave velocities are much

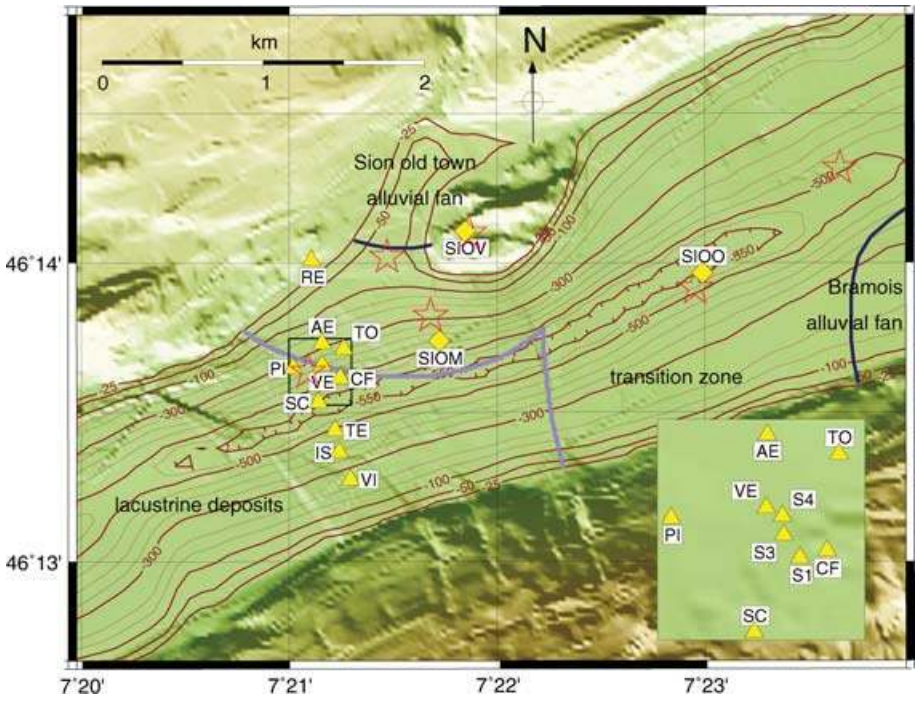

Figure 3. Bedrock depth (brown contours) and topography (colour shades) of the Sion area. Diamonds indicate the positions of the permanent strong-motion stations, triangles show receiver positions of the temporary array (station names are provided without the prefix 'SIO'). Darkblue and lightblue thick lines show the outline of alluvial fans and the transition zone, respectively. Stars are showing the central position of ambient noise array measurement performed in the area. Reproduced by permission of Swisstopo (BA081013).

higher at these sites, with values of more than 600 m s^{-1} measured close to the surface.

It is therefore important to include the type of the sedimentary deposit in the velocity model. We extracted the outline of the alluvial fans from geological maps of the central Valais area to define regions of higher shear wave velocities inside the sedimentary fill (Fig. 3).

Results from additional arrays recorded in the Sion area suggest that there is no sharp transition between fine lacustrine and coarse alluvial deposits. Shear wave velocities measured near the strong-motion station SIOO (Fig. 2d) and the temporary station SIOVE are not as large as those recorded on the top of the nearby alluvial fans but are clearly higher than those in the fine deposits encountered in Martigny and Vétroz (west of Sion). Borehole data available for the Sion area reveal alternating layers of coarse alluvial gravel and fine sands. This implies that the velocity decreases gradually with increasing distance from the alluvial fans. To obtain a smooth decrease between these two deposit types, a transition zone was introduced within a predefined distance of the fan boundaries (Fig. 3). Within this transition zone, the velocity decreases linearly with the shortest distance to the fan outline.

The depth of the sediment–bedrock interface was extracted from analogue maps published by Frischknecht & Wagner (2004) and Rosselli (2001). Fig. 3 shows contour lines of topography, bedrock depth and the positions of the permanent and temporary stations. The geophysical parameters of the different materials that compose our velocity model are listed in Table 1. Shear wave velocities of the sedimentary fill in our model are significantly lower than the constant 800 m s^{-1} used by Frischknecht *et al.* (2005), especially for the fine lacustrine and deltaic deposits. *P*-wave velocities in Table 1 are derived from seismic reflection results (Pfiffner *et al.* 1997), and densities are provided from gravimetric studies (Rosselli 2001). Quality factors are based on a velocity model developed by Steimen *et al.* (2003). The *P*-and *S*-wave velocity of the bedrock was taken from the literature (e.g. Maurer 1993; Baumann 1994).

Table 1. Geophysical parameters of the different materials in the velocity model. Depth ranges z are in m, velocities V in m s^{-1} and densities ρ in kg m^{-3}. Geological characterizations correspond to the interpretation by Pfiffner *et al.* (1997).

z	V_p	V_s	ρ	Q_p	Q_s	Geological interpretation
0–225	1700	700	1700	25	25	Alluvial fans
0–75	1600	320	1600	25	25	Deltaic sediments
75–225	1900	480	1900	25	25	Lacustrine deposits
225–400	1900	750	1900	25	25	Glaciolacustrine deposits
400–500	1900	800	1900	25	25	Meltout and reworked till
500–560	2000	900	2000	25	25	Subglacial deposits
0–750	4000	2325	2500	100	100	Bedrock

3 METHOD

3.1 Weak motion records

A temporary network of up to 13 weak–motion seismometers was installed in the town of Sion to quantify the level of amplification. The temporary network was operative during two recording periods—the first installation was maintained from April 2004 to October 2004; the second deployment lasted from June 2005 until April 2006. The first deployment consisted of 13 stations, while only nine seismometers were available for the second installation (Table 2). Additionally, the two permanent strong-motion stations

Table 2. Positions of permanent strong-motion accelerometers and temporary weak-motion seismometers. The last column shows the deployment period of the stations (1: first recording period from 2004 April to October, 2: second period from 2005 May to 2006 April).

Station	Longitude (°E)	Latitude (°N)	Elevation (m)	Sensor	Network
SIOV	7.364098	46.235095	558	ES-T	2
SIOO	7.383156	46.232776	495	ES-T	2
SIORE	7.351785	46.233476	514	3D/5s	1
SIOAE	7.352648	46.228850	488	3D/5s	1,2
SIOVE	7.352625	46.227627	487	3D/5s	1,2
SIOTO	7.354382	46.228524	488	3D/5s	1,2
SIOPI	7.350330	46.227448	486	3D/5s	1,2
SIOCF	7.354086	46.226901	489	3D/5s	1,2
SIOS1	7.353442	46.226784	488	3D/5s	1
SIOS3	7.353045	46.227164	488	3D/5s	1
SIOS4	7.353013	46.227484	488	3D/5s	1
SIOSC	7.352339	46.225536	486	3D/5s	1,2
SIOTE	7.353680	46.223987	485	3D/5s	1,2
SIOIS	7.354006	46.222773	486	3D/5s	1,2
SIOVI	7.354915	46.221244	485	3D/5s	1,2

SIOV and SIOO were upgraded with continuous 24-bit digitizers to complement the second temporary network.

All temporary stations were equipped with Lennartz 3-D/5s seismometers with a natural period of 5 s; the strong-motion stations SIOO and SIOV use an Episensor ES-T force-balance accelerometer, which has a flat response between DC (direct current) and 50 Hz. This configuration allows us to analyse the deep resonance of the basin, which is expected at periods longer than 1 s (Frischknecht *et al.* 2005). The sampling rate was set to at least 100 samples per second. GPS signals were used for time synchronization.

The temporary station SIORE was deployed on a well-defined bedrock site on the northern margin of the basin and will be used as a reference station for the first deployment period; for the second installation the strong-motion station SIOV will serve as reference site.

Six of the temporary receivers (SIOAE, SIOVE, SIOSC, SIOTE, SIOIS and SIOVI) were arranged along a profile running perpendicular to the valley axis (Fig. 3) to study the variability of the amplification with distance from the valley edges. Three more stations (SIOTO, SIOCF and SIOPI) were installed on the north side of the profile to form a roughly circular array. For the first installation, the network was complemented with an inner array (SIOS1, SIOS3 and SIOS4) to improve the resolution of frequency-wavenumber methods at higher frequencies (enlarged section in Fig. 3).

Since the seismicity in the region is quite moderate and the noise level in the city was rather high, only few earthquakes provided an useful signal-to-noise ratio in the frequency range of interest (0.2–10 Hz). Table 3 lists the source parameters of the events discussed in this text.

During the first recording period in 2004, a sequence of more than 170 detected events occurred near Derborance, at 14 km epicentral distance from Sion (Baer *et al.* 2005). For this study, we will use the four strongest events of the sequence, which reached magnitudes between 2.4 and 2.9 (Table 3). Additionally two events with local magnitudes of 3.8 and 4.0 occurred in northern Switzerland, within 155 km epicentral distance of the network, which provided useful signals. We will also analyse two events with magnitudes of 4.2 and 3.3 located in northern Italy at 125 and 66 km epicentral distance, respectively.

During the second deployment period, on 2005 September 8, a M_{L} 4.9 event occurred near Vallorcine (France), at an epicentral distance of 43 km from the array (Deichmann *et al.* 2007). Fig. 4 compares seismograms from stations located on the unconsolidated sediments, including the reference station. Two aftershocks, which reached a magnitude of ∼3.0, will also be included in the analysis. Unfortunately, the station SIOSC in the valley centre was not operative during this series. Four more events with local magnitudes between 3.7 and 4.1 were recorded within a radius of 155 km of the network (Table 3); additionally, a local M_{L} 2.6 event was detected 12 km SE of Sion. All available signals from the events given in Table 3 will be used to estimate amplification levels.

3.2 3-D finite difference simulations

The seismic response of the Sion basin was simulated with the 3-D finite difference method using a code developed by Olsen (1994). The 3-D viscoelastic equations of motions are solved with the staggered-grid Velocity–stress finite-difference scheme; the accuracy is fourth order in space and second order in time. Viscoelasticity is modelled

Table 3. Characteristics of the events recorded on the temporary network.

ID	Origin time	Lon. (°E)	Lat. (°N)	Mag. (M_L)	Location	AZ (°)	Δ (km)
D1	2004.05.03 23:14	7.2	46.3	2.4	Derborance, VS	305	14
I1	2004.05.14 00:30	7.33	45.10	4.2	Condove, I	181	125
D2	2004.05.30 07:20	7.191	46.284	2.7	Derborance, VS	297	14
D3	2004.05.30 09:46	7.193	46.284	2.9	Derborance, VS	297	14
I2	2004.06.12 04:44	6.947	45.717	3.3	Pré St. Didier, I	209	66
D4	2004.06.12 16:47	7.197	46.276	2.6	Derborance, VS	294	14
N1	2004.06.21 23:10	7.713	47.505	3.8	Liestal, BL	11	143
N2	2004.06.28 23:42	8.169	47.525	4.0	Brugg, AG	23	155
V1	2005.09.08 11:27	6.897	46.032	4.9	Vallorcine, F	238	43
V2	2005.09.08 11:53	6.905	46.031	3.0	Vallorcine, F	237	43
V3	2005.09.08 14:10	6.897	46.033	2.9	Vallorcine, F	238	43
F1	2005.10.31 03:40	6.41	45.72	3.7	Albertville, F	233	91
N3	2005.11.12 19:31	8.166	47.523	4.1	Brugg, AG	23	155
I3	2005.11.20 10:48	8.96	45.40	4.1	Milan, I	126	155
F2	2006.01.11 10:32	5.44	45.93	4.1	Blanaz, F	258	147
L1	2006.03.18 22:49	7.50	46.21	2.6	Vissoie, VS	99	12

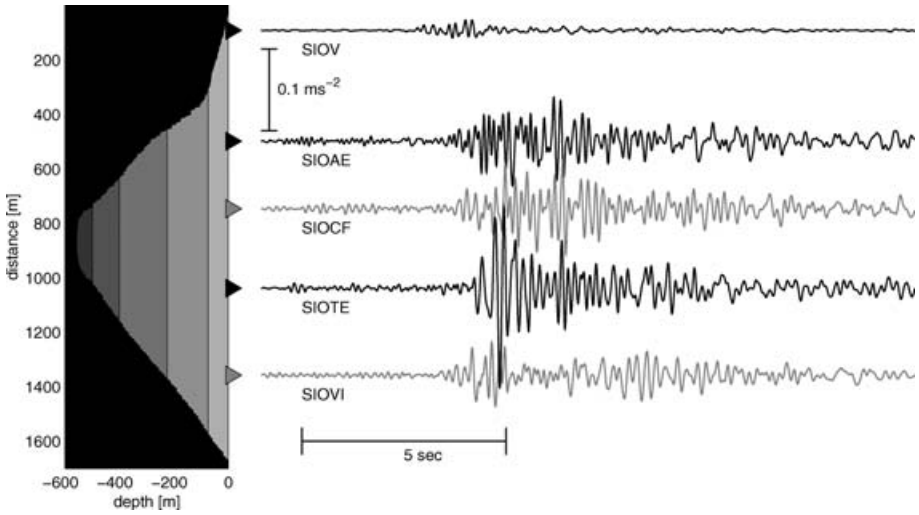

Figure 4. Accelerograms on reference site (top) and on the Rhône sediments recorded after the M_L 4.9 Vallorcine main shock. Seismograms were rotated to the direction perpendicular to the valley axis and low-pass filtered below 5 Hz.

with a coarse-grained implementation of the memory variables for a constant Q solid.

The geophysical model (Table 1) was discretized with a grid spacing of 12.5 m, which allows us to propagate frequencies up to 4 Hz using 6.4 gridpoints for the shortest shear wavelength. At the sides of the computational domain, we applied absorbing boundaries of 20-gridpoints width, which were padded with an attenuative material (Cerjan *et al.* 1985).

The full model consists of 450 × 360 × 80 nodes and covers a volume of 5625 × 4500 × 1000 m^3. The section shown in Fig. 3 corresponds to the surface of the computational area without the absorbing boundaries. Topography is not implemented in the finite-difference scheme, and the outcropping bedrock represents a plateau at the elevation of the basin surface in our velocity model.

The simulations were run on a 128-processor 2.4 GHz Linux cluster at San Diego State University. We simulated 20 s of wave propagation using a time step of 0.0015 s. With this configuration, one computation requires about 8 hr wallclock time using 20 CPUs.

In this study, we will focus on modelling the response of the basin to four observed earthquakes. Since the hypocentres of those sources are far away from the computational area, we specified the sources by imposing seismograms along the bottom plane of the grid. The input signal on each gridpoint was delayed by the shear wave traveltime of the bedrock and the corresponding direction of incidence to generate a plane wave. We used seismograms of the selected events recorded on permanent broad-band stations (of the Swiss Digital SDSNET) as input velocity. The seismograms were low-pass filtered with a corner frequency of 3.5 Hz with a third-order two-pass butterworth filter.

We simulated four of the observed earthquakes to analyse the valley response to waves arriving from different directions. The main shock of the Vallorcine sequence (V1 in Table 3) was modelled with the signal from the permanent broad-band station DIX, which is located south of Sion (Fig. 1). Fig. 5 shows snapshots of simulated ground velocities which are discussed below. We also modelled the strongest M_L 2.9 event (D3) of the Derborance series. For this simulation seismograms acquired on the temporary station SIORE were used as input signal. The M_L 4.0 event of Brugg (N2) was simulated to represent the three events located in northern Switzerland, using a record from the broad-band station WIMIS north of Sion. For the simulation of event I3, the seismogram recorded on the broad-band station DIX served as input signal.

Additionally we simulated the historical M 6.1 Sierre earthquake of 1946 January 25. Wanner (1955) determined the location of the main shock from the few stations that were operating at that time. The epicentre was determined at 46°19′N and 7°30′E, ∼15 km E–NE of Sion (Fig. 1). Macroseismical estimations yield a depth of about 12 km (Fäh *et al.* 2003), which is similar to the depth of 10 km reported by Wanner (1955).

The orientation of the aftershock zone as as well as macroseismical observations suggest that the 1946 earthquake ruptured from east to west on the northern side of the Rhône valley (Wanner 1955). The exact source mechanism is not known.

Because no records are available, we queried the European strong-motion database (Ambraseys *et al.* 2001) for a signal with a comparable frequency content. We chose a seismogram of the 1976 M_s 6.5 Friuli earthquake recorded at the station Tolmezzo-Diga Ambiesta, a rock site located 23 km from the rupture. As with the other simulations, the source was implemented with a plane wave arriving from the hypocentral direction. To match the lower magnitude of the 1946 earthquake, the input signal would need to be reduced first. However, since we will focus on amplification of Fourier spectra and peak velocities caused by the basin, the amplitudes are instead normalized by the reference station.

3.3 Analysis of signal-to-noise ratio

Since the noise level in the city is significantly higher than on the two reference sites, the signal-to-noise ratio at each station needs to be considered to prevent local noise sources from polluting spectral ratios. We computed the ratio of pre-event to event spectral amplitudes on both horizontal components for each station and each event. Only events with a signal-to-noise ratio above 2 (i.e. a pre-event to event ratio of at least 3) in the frequency range between 1 and 10 Hz were considered in our analysis (Table 3).

3.4 Estimation of Fourier amplification

We investigate site amplification in the Fourier spectral domain on both horizontal components using the same procedure for synthetic

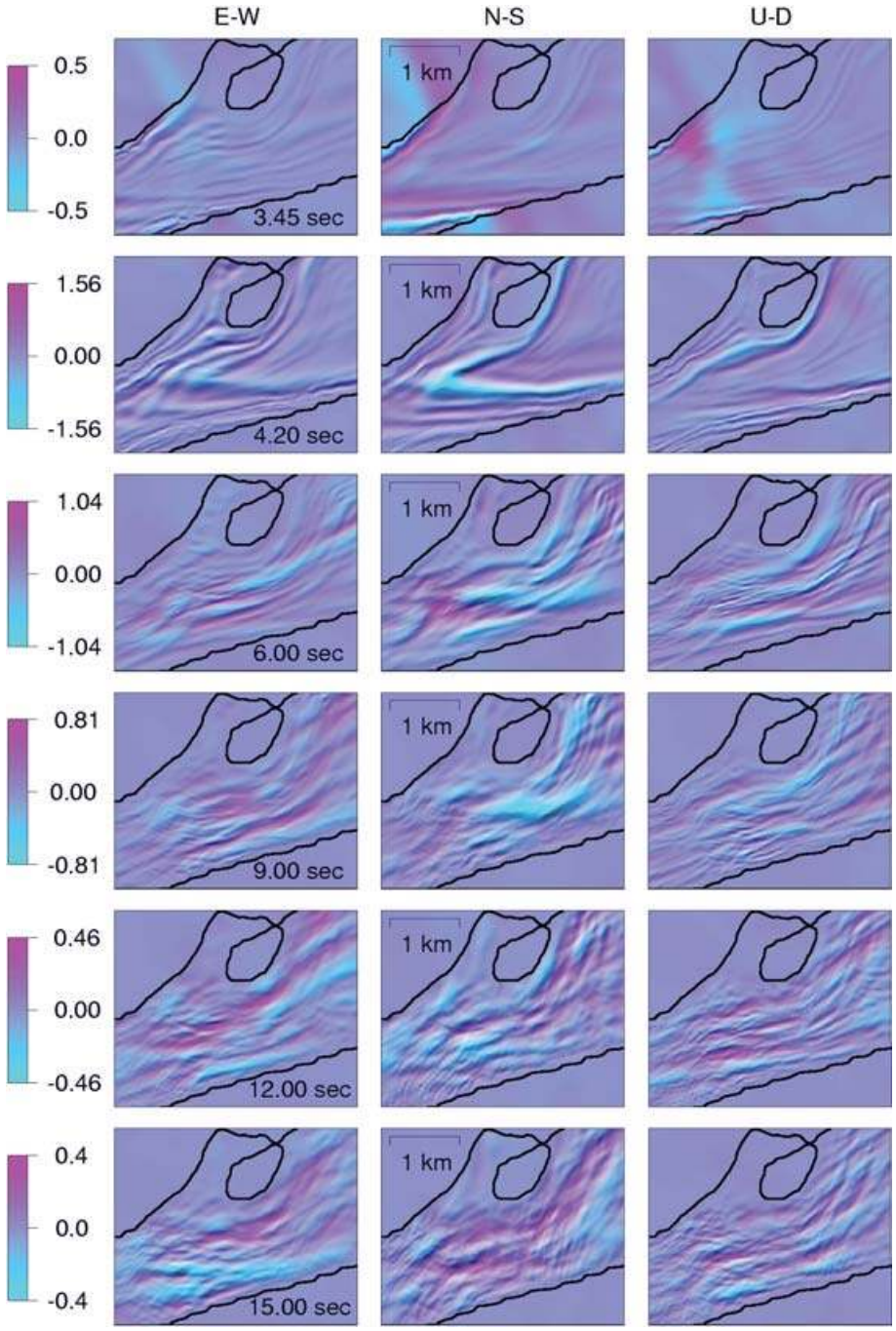

Figure 5. Snapshots of simulated wave propagation in the Sion basin after excitation with a plane wave corresponding to the Vallorcine main shock. Velocities are in 10^{-2} m s^{-1}; the scale is time-dependent.

and simulated ground motion. Seismograms were converted to acceleration in m s^{-2} to allow comparison with the two strong-motion receivers. We removed the mean, applied a trapezoidal taper and selected a window containing the intense *S*-wave part of the seismograms. To increase resolution of the discrete Fourier transform at lower frequencies, the extracted signals were zero-padded to 2^{14} samples. The amplitude spectra of the Fourier transform were smoothed using the window proposed by Konno & Ohmachi (1998) with a bandwidth of 20 samples. Finally the total spectral amplitude in the horizontal direction was computed and divided by the Fourier amplitude of the reference station. For computation of average Fourier amplifications of all events, we discarded frequencies with signal-to-noise ratios below the threshold.

3.5 Frequency-wavenumber analysis

We apply frequency-wavenumber methods on recorded and simulated ground motion to estimate the direction of arrival and velocity of wave trains propagating through the basin. Results shown in this text were acquired with the high-resolution frequency-wavenumber technique (Capon 1969) and the multiple signal characterization (MUSIC) method developed by Schmidt (1986a,b). A description

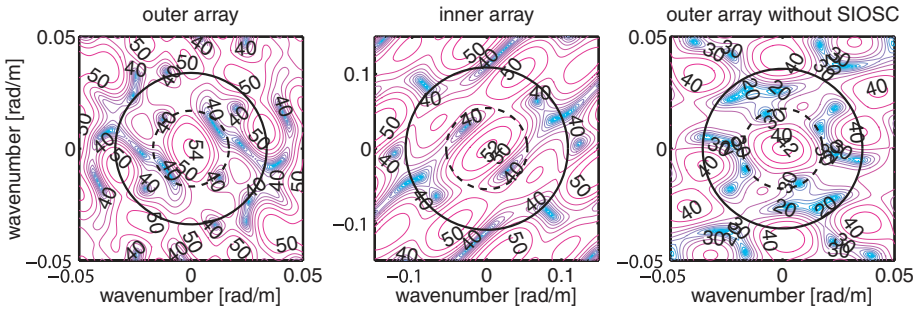

Figure 6. Array response beampatterns for the outer and inner temporary arrays and for the outer array without the station SIOSC. The solid rings reflect the location of the first aliasing peaks, and the wavenumber domain that can be analysed is within the dashed rings. Contours show the array output in dB.

of these methods can be found in Zerva & Zhang (1996) or Hartzell *et al.* (2003). We used the routines provided by the geopsy software package (Ohrnberger *et al.* 2004) and adapted them for processing of interactively selected time windows.

From the *f*–*k* spectra computed with the high-resolution method, only the slowness and direction of the maximum array output was picked. The MUSIC algorithm is able to resolve multiple sources, but one difficulty is that the number of sources present in the signal must be known or estimated. We followed the minimum descriptive length (MDL) criterion (Wax & Kailath 1985), which is implemented in the geopsy routine, to determine the maximum number of sources. However, it has been shown that this method may induce an overestimation of the number of sources if the time windows are short (Marcos 1998). Therefore, we only considered multiple sources determined by the MUSIC algorithm if the *f*–*k* map produced by the high-resolution method indicated more than one direction of origin.

Fig. 6 shows the resolution beampatterns for the large outer array and the small inner array that was recording during the first installation period. The position of the receivers was pre-determined by the distribution of buildings and the availability of power supplies, and it was not possible to achieve an ideal array configuration for the inner ring. The failure of the station SIOSC during the Vallorcine series has little impact on the array resolution capabilities (Fig. 6 right-hand panel). Fig. 7 compares the array resolution limits with Rayleigh wave phase velocities measured near the array centre. The lower resolution limit was computed using a maximum wavelength of twice the array aperture. Only a narrow frequency band can be analysed with each array. We chose to perform the *f*–*k* processing at about 1.25 Hz with the outer array and at 2.5 Hz with the inner array; the observed phase velocities are well below the aliasing limits at these frequencies.

For *f*–*k* analysis of the simulated ground motion, we extracted synthetic seismograms on gridpoints belonging to circular arrays. The array geometry was chosen to match the analysed frequency band; we used a radius of 150 m (12 gridpoints) and 50 m (4 gridpoints) for processing at 1.25 and 2.5 Hz, respectively.

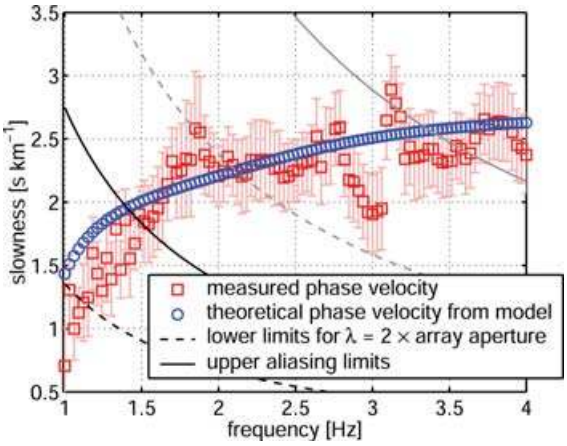

Figure 7. Array resolution limits for the outer (black) and inner (grey) arrays. The measured phase velocities (errorbars) were derived from ambient noise recorded in the vicinity of the station SIOVE. The theoretical phase velocity was computed from a 1-D column through the velocity model at the array centre.

4 OBSERVED AND SIMULATED FOURIER AMPLIFICATIONS

In this section, we will show Fourier amplifications of the events from Table 3. The events from the Derborance and Vallorcine series are analysed together because similar results are expected from the almost identical location and source mechanism.

4.1 Vallorcine series

The M_L 4.9 main shock (V1 in Table 3) and two aftershocks (V2 and V3) were recorded on eight receivers of the temporary network.

Fig. 8 shows observed site-to-reference spectral ratios from the main event and the two aftershocks. Despite the different signal-to-noise ratios, all three events yield very similar amplifications for frequencies below 10 Hz. At all stations but SIOAE and SIOTO, a first peak can be identified between 0.4 and 0.7 Hz, with the largest amplification of approximately 10 obtained at the station SIOIS. At most sites, the highest amplitude is reached between 2 and 10 Hz. The most prominent peak can be seen at the station SIOTE for a frequency of 3.5 Hz, where the amplitude reaches a factor of 19. All sites exhibit significant amplifications near this frequency. At the site SIOAE, another significant amplification peak appears at about 9 Hz.

In Fig. 8, the observed Fourier spectral ratios are compared with spectral ratios computed from synthetic signals. At all stations, the synthetic spectral ratios show a first peak at about 0.5 Hz and increase again above 2 Hz. The simulated site response is very close to the observations for the stations SIOO, SIOTE and SIOIS. At all sites except SIOO, the fundamental frequency is slightly underpredicted by the simulation. The simulated transfer function for the station SIOTO yields twice the value of the observations at 0.6 Hz. This could imply that this station is located outside the deeper part of the

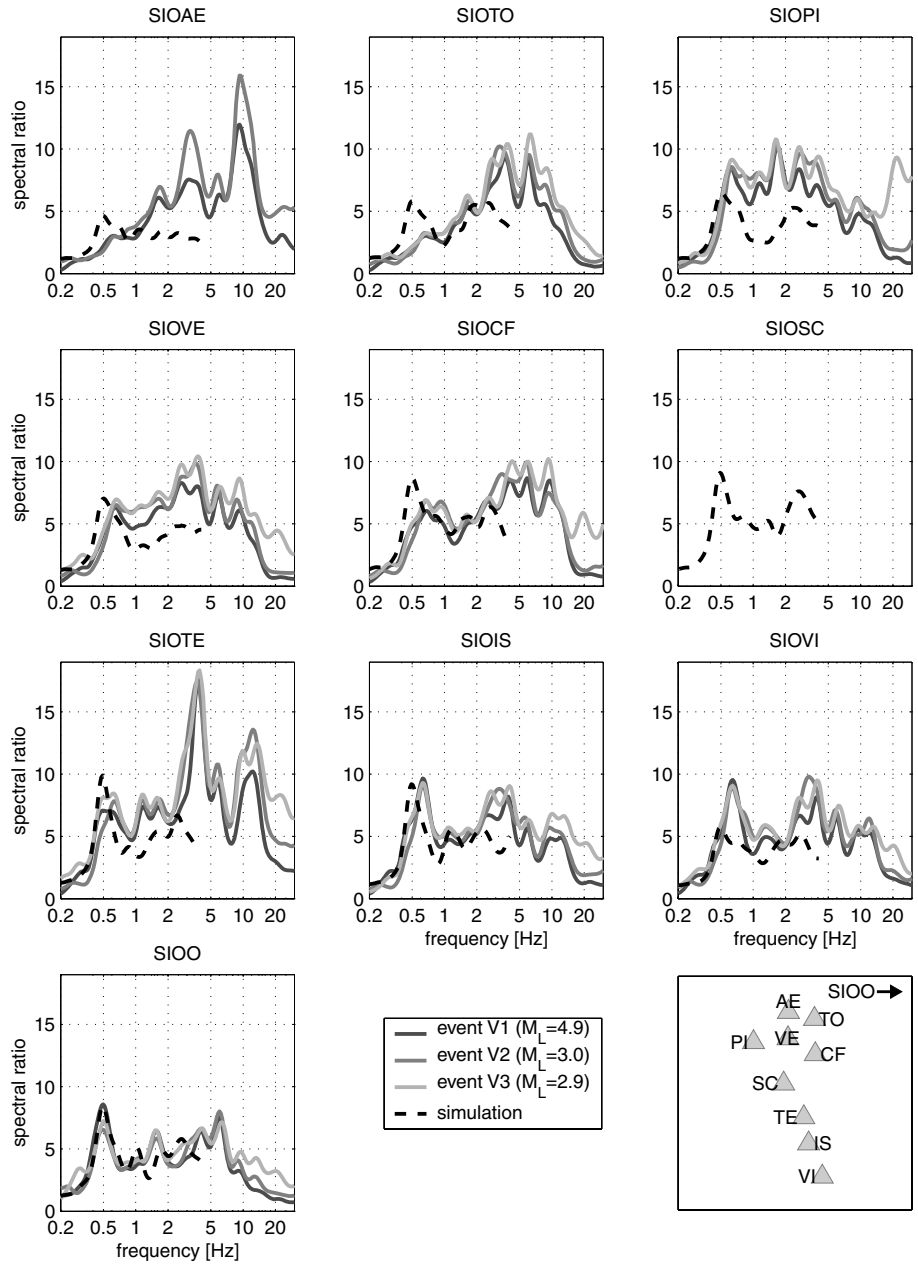

Figure 8. Observed (solid) Fourier spectral ratios computed from seismograms of the Vallorcine series (Table 3). The black dashed line shows Fourier spectral ratios computed from synthetics of the Vallorcine simulation. The relative station positions are indicated on the lower right-hand side plot, with the prefix 'SIO' stripped from station names.

basin, or that shear velocities are higher than those in our structure model.

4.2 Derborance series

During the Derborance series, the first temporary network with 13 weak motion instruments was recording. At the station SIOTE no signals were recorded for events D2–D4. We will not show spectral ratios acquired on the inner array stations SIOS1–SIOS4, because they are very similar to those acquired at the site SIOCF. Spectral ratios computed from signals of the Derborance sequence (D1–D4) are given in Fig. 9. The four events are yielding similar Fourier amplifications at frequencies above 2 Hz for a given site, and all stations show a peak at about 2.8 Hz. Amplifications at the fundamental frequency of 0.6 Hz are showing a greater variability due to the lower signal-to-noise ratio, especially for the stations SIOPI and SIOVI. Synthetic spectral ratios are also exhibiting a fundamental peak, though at a lower frequency of 0.45 Hz and with generally higher amplitudes.

4.3 Northern Switzerland events

Three of the recorded events (N1–N3 in Table 3) occurred in northern Switzerland at comparable epicentral distance and azimuth. During the last event the strong-motion, station SIOV did not provide useful signals; we will therefore use the permanent broad-band

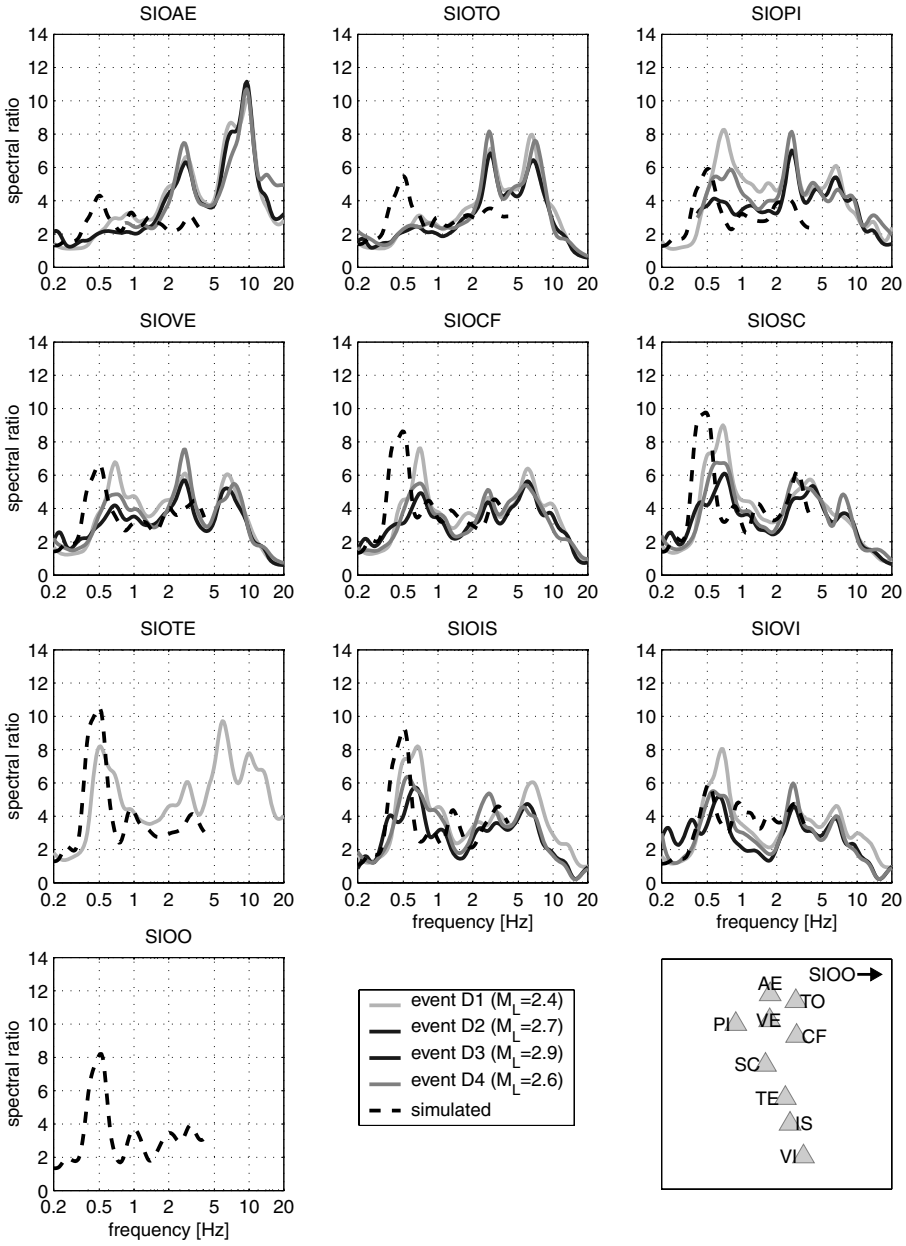

Figure 9. Observed (solid) and simulated (dashed) Fourier spectral ratios for Derborance series (D1–D4).

station SENIN as reference site. The observed spectral ratios from the three events (Fig. 10) show larger variability at a given site than those of the Derborance and Vallorcine sequences (Figs 9 and 8), though most spectral ratios show a fundamental frequency of 0.6 Hz and a second amplification at about 2.5 Hz. Simulated spectral ratios are exhibiting a first peak at about 0.5 Hz and secondary peaks at frequencies above 1 Hz.

4.4 Site characterization

We computed average Fourier amplifications from the observed and simulated events to characterize the station sites of the temporary network (Fig. 11). The signal-to-noise ratio was computed for each station, and only frequencies with a ratio above the threshold were considered to compute the average amplification. In general, more events were available at frequencies above 1 Hz due to the better signal-to-noise ratio.

At most sites, average Fourier spectral ratios reach a level of at least 5 in the frequency range between 1 and 10 Hz. The deep resonance of the basin at 0.6–0.7 Hz is clearly visible at the stations SIOCF to SIOVI and SIOO.

Simulated average spectral ratios are able to reproduce the fundamental deep valley response, tough the fundamental frequency is underestimated at the stations SIOVE, SIOCF and SIOSC. At most sites, simulated average amplifications are within the standard deviation of the observations. The discrepancies between the observations and simulations at stations SIOTO and SIOAE show that the velocity model needs to be improved in that region.

5 DEEP VALLEY RESPONSE

Site-to-reference spectral ratios computed from observed events exhibit a fundamental frequency at about 0.6 Hz at all stations except SIOAE (Figs 8–10), regardless of the position on the basin and the

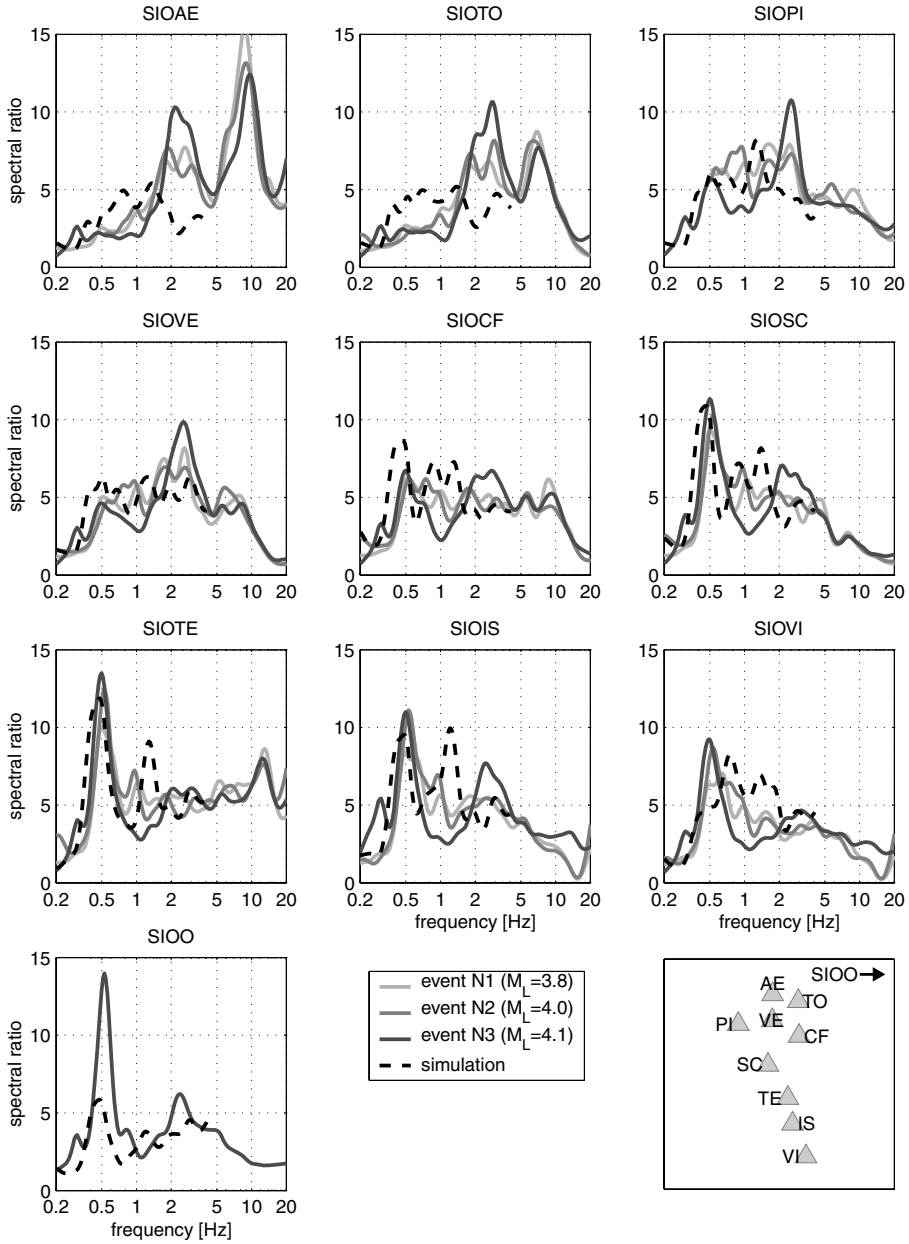

Figure 10. Observed (solid) and simulated (dashed) Fourier spectral ratios for northern Switzerland events (N1–N3).

local sedimentary thickness. This is characteristic for the case of 2-D resonance, which has been predicted for deep embanked valleys with a high velocity contrast. As Bard & Bouchon (1985) showed from computations with the Aki-Larner technique, 2-D resonance results in a fundamental frequency of amplification, which is insensitive to the position in the valley but which produces the highest amplification near the basin centre. This is different from the 1-D response, which is frequently observed in shallow valleys where the observed fundamental frequency reflects the local sedimentary thickness.

Bard & Bouchon (1985) introduced the equivalent shape ratio as a simple criterion to distinguish between shallow valleys, dominated by 1-D resonance and lateral propagation, and deep valleys, dominated by 2-D resonance. The equivalent shape ratio corresponds to the maximum valley depth divided by the width over which the sediment thickness is more than half its maximum value. The critical shape ratio decreases with increasing velocity contrast between sediment and bedrock (Fig. 12).

We calculated the equivalent shape ratios from the sediment–bedrock interface in the velocity model for cross-sections at the temporary network and at the station SIOO. The shear velocity contrast was computed with the traveltime-based average from soil columns taken through the velocity model (Table 1) at the stations SIOSC and SIOO. For the temporary network, a shape ratio of 0.7 and a velocity contrast of 5.0 are obtained, which places the site well inside the domain of 2-D resonance (Fig. 12). Even if the shear-velocities were as high as 900 m s^{-1} for the whole sediment fill (errorbars in Fig. 12), the equivalent shape ratio would still be above the critical value. For the cross-section at the station SIOO, the shape-ratio and velocity contrast are slightly lower, yet the site is still clearly located in the area where the development of 2-D resonance must be expected. In a previous study, we have analysed ambient noise recorded at similar

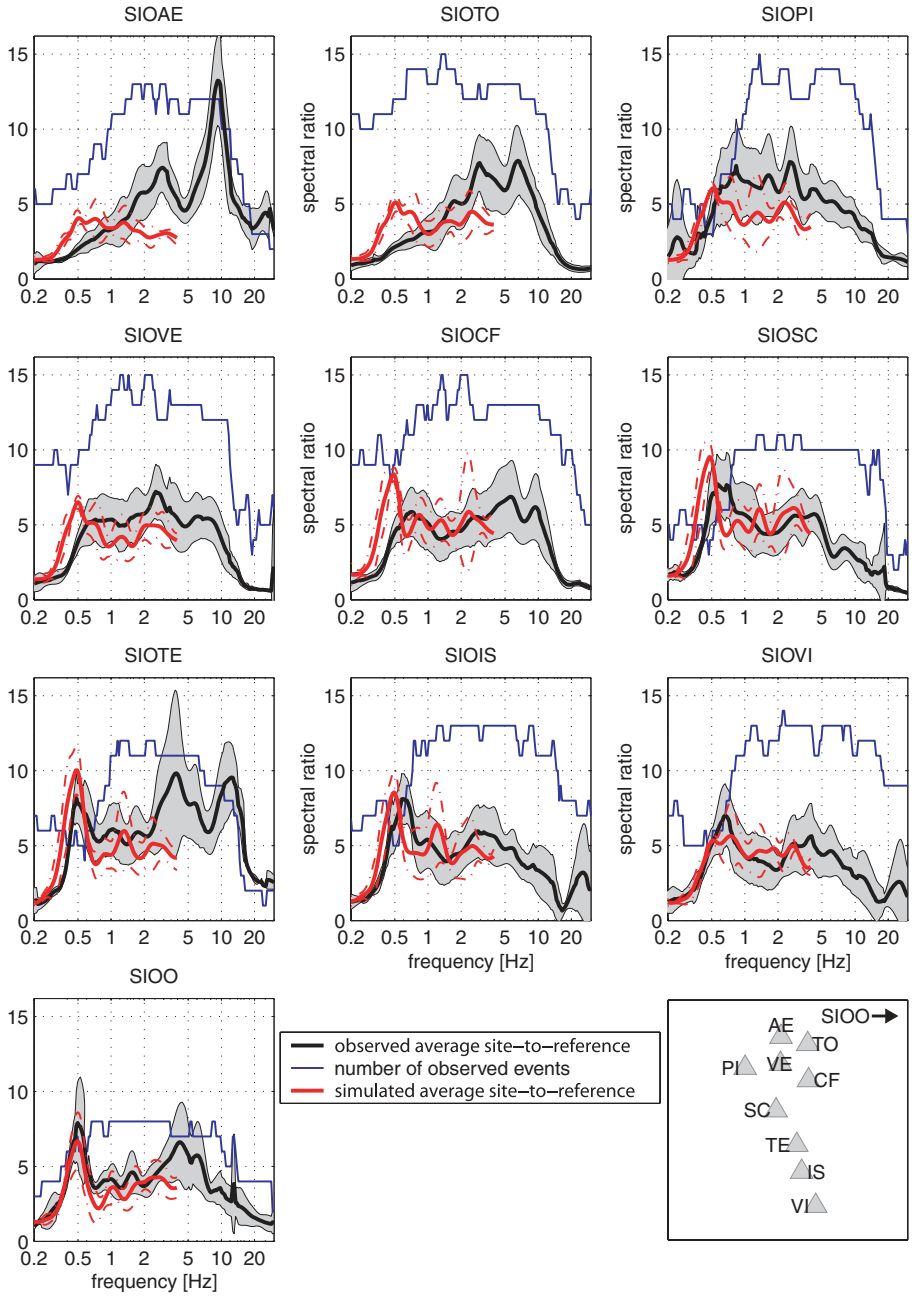

Figure 11. Comparison between average observed (bold black lines) and average simulated (bold red lines) Fourier amplification at the temporary stations. Standard deviations are indicated by the grey patch (observed) and dash–dotted red lines (simulated). Blue lines depict the number of recorded earthquakes used to compute the average amplification at each frequency.

sites in the Rhône valley (Roten *et al.* 2006; Roten & Fäh 2007), and we suggested that observations in site-to-reference spectral ratios can be explained in terms of 2-D resonance.

2-D resonance involves three different modes, the *SV*, *SH* and *P* mode. The *SH* mode involves particle motion parallel to the valley axis (axial direction), the *SV* mode produces particle motion in the direction perpendicular to the valley axis and on the vertical component. Both *SH* and *SV* mode show a maximum amplification in the valley centre on the horizontal components.

These different modes can be distinguished if the horizontal components are rotated to the axial and perpendicular direction of the valley. Fig. 13 shows spectral ratios computed from synthetics of event N3 as a function of distance on a profile across the basin. On the axial component, a first peak appears at about 0.42 Hz at all receivers, regardless of the position along the profile axis. The amplification at this frequency reaches a maximum near the valley centre. These observations are in agreement with the behaviour expected for the SH_{00} fundamental mode of 2-D resonance. On the direction perpendicular to the valley axis, the SV_0 fundamental mode can be identified at about 0.50 Hz.

In Fig. 14, the same analysis is done for recorded seismograms from event N3. The main characteristics of recorded spectral ratios match the pattern inferred from the simulations, though the observed resonance frequencies are a bit higher. On the axial component the

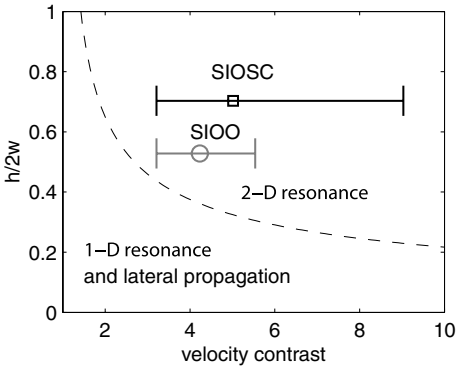

Figure 12. Critical shape ratio (dashed) as a function of the velocity contrast for the SH case. The shape ratios for the Rhône basin near the stations SIOSC (black) and SIOO (grey) are plotted for the corresponding velocity contrast, which was computed from a 1-D soil column below the respective station. Errorbars are indicating the velocity contrast for the minimum and maximum shear velocities inside the sediment fill. (Modified from Bard & Bouchon 1985).

SH_{00} fundamental mode is visible at 0.55 Hz for most stations, and the fundamental mode SV_0 can be observed at 0.59 Hz on the perpendicular and vertical axis.

We carried out the above analysis for all recorded and simulated events and defined the frequencies of modes SH_{00} and SV_0 (Table 4). The frequencies of these modes appear to be sensitive to the analysed event. Observed values range between 0.45 and 0.55 Hz for SH_{00} and between 0.59 and 0.70 Hz for SV_0. These differences are probably caused by 3-D effects of the complex basin structure. However, for each individual event, the frequencies are constant along the profile and do not depend on the local sedimentary thickness, as expected in the case of 2-D resonance. Earthquakes with similar source location and mechanism yield similar resonance frequencies, as can be seen from observations of the Vallorcine (V1–V3) and Derborance (D1–D4) series.

Additionally, we determined the 2-D resonance frequencies from ambient noise using a 1 hr window of undisturbed nighttime records (entry termed NS in Table 4). The identified fundamental frequencies compare well with those found from the weak motion signals,

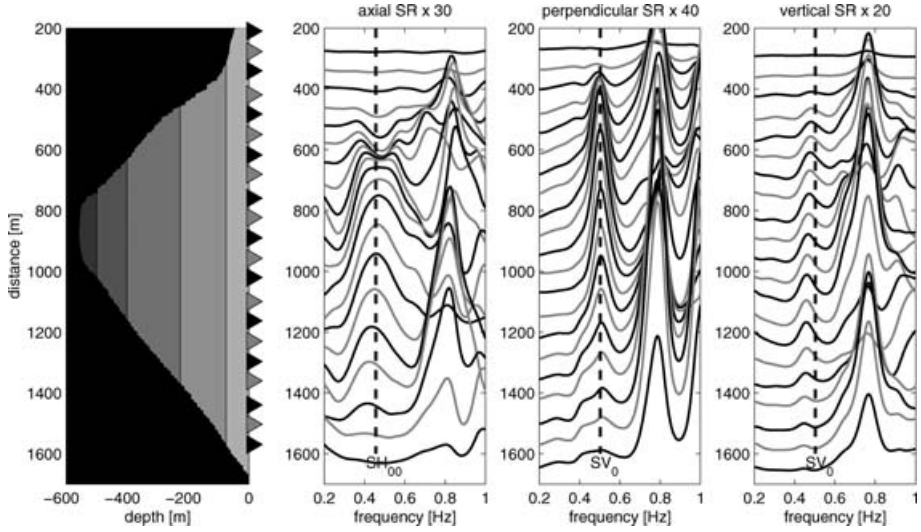

Figure 13. Spectral ratios computed from synthetics of event N3 for all components as a function of distance across the basin. Scale factors of 30, 40 and 20, respectively, were applied on spectral ratios. The cross-section through the velocity model is displayed for orientation.

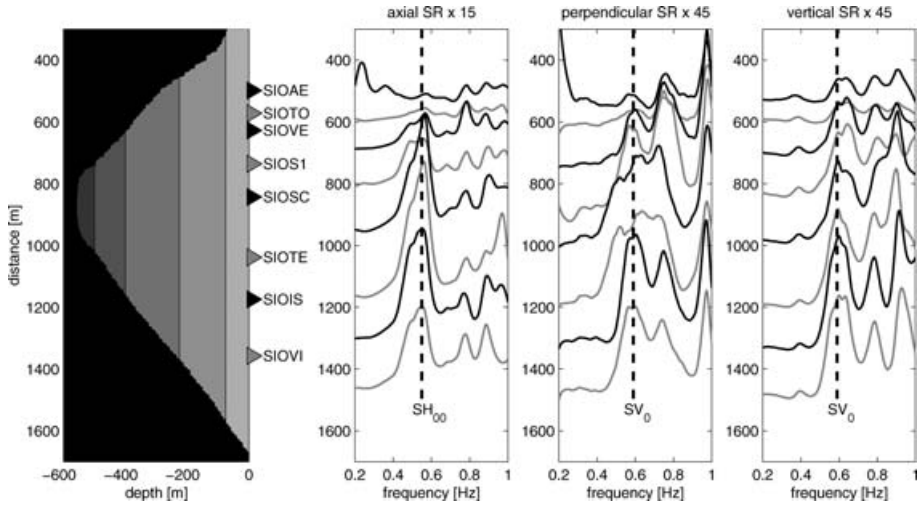

Figure 14. Like Fig. 13, but for recorded seismograms of event N3.

Table 4. Fundamental mode 2-D resonance frequencies identified from all observed events. The last entry (NS) shows the resonance frequencies determined from ambient noise.

Ev.	SH_{00}	SV_0
D1	0.52	0.70
D2	0.55	0.63
D3	0.53	∼0.68
D4	0.53	∼0.68
V1	0.45	0.62
V2	0.48	0.67
V3	0.48	0.63
N1	0.50	0.64
N2	0.55	0.59
N3	0.45	0.62
I1	0.48	0.61
I2	0.48	0.65
I3	0.50	0.61
F1	0.48	∼0.67
F2	0.46	0.61
L1	0.47	∼0.51
NS	0.52	0.60

Table 5. Fundamental mode 2-D resonance frequencies identified from the simulated ground motion.

Sim.	SH_{00}	SV_0
D3	0.44	0.50
V1	0.42	0.52
N2	0.45	0.50
I3	0.47	0.53

which confirms that ambient vibrations may be used to identify 2-D resonances (Roten *et al.* 2006).

Resonance frequencies determined from the simulated ground motion are also showing some variability with respect to the simulated incoming wavefield (Table 5), though not to the extent observed in the recorded earthquakes. This might be explained with the very simple source configuration used for our simulations, which is not able to reproduce the incoming wavefield at its full complexity, or with the limited accuracy of the velocity model.

The 2-D resonance frequencies defined from the simulations are always lower than the observed values, with 0.42–0.47 Hz for SH_{00} and 0.50–0.53 Hz for SV_0. This implies that shear wave velocities in the sedimentary fill could be higher than those in our velocity model, or that the 3-D structure within the basin fill is more complicated. Another source of uncertainty is the geometry of the sediment–bedrock interface below the temporary network since it was mainly interpolated from nearby gravimetric and seismic surveys.

6 FREQUENCY-WAVENUMBER ANALYSIS

To determine the direction of arrival of waves propagating through the array, we applied the *f–k* techniques described above to the vertical component of recorded and simulated seismograms. We will show results of the M_L 4.9 Vallorcine main shock (V1) and the M_L 4.0 Brugg event (N2).

6.1 Vallorcine main event

Because no inner array was available during this event, we will limit the analysis to the frequency 1.10–1.25 Hz. For analysis of synthetic ground motion we used a circular array consisting of two rings with radii 150 and 75 m, respectively, centred at the same location as the real network. We selected five time windows of ∼4 s length from the synthetic seismograms (Fig. 15 left-hand panel).

The first time window (a) contains only the first arrival; both the high-resolution and MUSIC technique resolve an azimuth of about 240° and a slowness of ∼0.4 km^{-1} s (2500 $m\,s^{-1}$). This is consistent with a body wave originating from the azimuth of the simulated event.

The next time window (b) yields an azimuth of 330° and a slowness of about 2 km^{-1} s (500 $m\,s^{-1}$), which is close to the theoretical Rayleigh wave phase velocity at 1.25 Hz, computed from the geophysical model (Fig. 7). This identifies the phase as a Rayleigh wave generated at the basin edge northwest of the array centre. The next two time windows (c and d) show a very similar pattern; the last window (e) shows surface waves originating southeast of the site. Additionally, MUSIC identifies a signal propagating from the northwest. Therefore, edge-generated surface waves originating from both sites are dominating the simulated wavefield (Fig. 5). This can also be seen very clearly in animations of the simulated earthquake scenario (see Supplementary Material in the online version).

Fig. 16 shows results of the *f–k* processing applied on the recorded ground motion. The record length of the observed time-series are longer than the simulations, which allows us to use more and longer time windows. Again, the first arrival (time window a) corresponds to a body wave arriving from the direction of the epicentre (Fig. 16). The time windows b and c show edge-generated surface waves originating in the northwest to north, deviated by ∼30° from the directions observed in the simulations.

Analysis of the remaining time windows reveals surface waves arriving from almost all directions. The phase slowness of these surface waves is generally 20–25 per cent lower than in the simulation. As we observed earlier, this suggests that shear wave velocities near the array centre are higher than the values used in the velocity model.

6.2 Northern Switzerland event N2

The M_L 4.0 event of Brugg was recorded during the first deployment period, for which the inner array is available. Therefore, the analysis can be performed at both 1.25 and 2.5 Hz. This is especially interesting because site-to-reference spectral ratios determined from the northern Switzerland events (N1–N3) show significant peaks of amplification at about 2.5 Hz for most stations.

Fig. 17 shows the selected windows and directions of origin derived from the simulation of event N2. At both frequencies, the first arrivals are arriving from the north, deviated by about 30 degrees from the direction to the epicentre. Arrivals from this direction can also be seen on later time windows, since the basin was excited during the whole simulation length. Additionally, surface waves arriving mainly from the N–NW and SE are resolved. More different phases can be identified at 2.5 Hz because the shorter period allows to use a larger number of time windows.

Snapshots of the simulated surface velocity show that the first arrivals consist of surface waves generated on the northern margins of the basin (Fig. 18 top). Edge-generated surface waves from the NE appear on later snapshots.

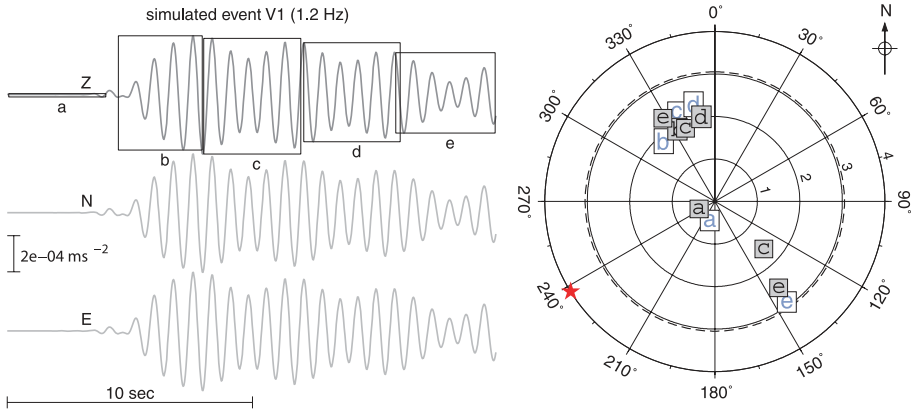

Figure 15. *Left-hand panel* Time windows for *f–k* analysis selected from a simulated seismogram at the array centre. The synthetics have been bandpass filtered around the frequency of *f–k* analysis (1.25 Hz). *Right-hand panel* Estimated slowness and direction of origin of signals for the different time windows. Slowness is in seconds per kilometre. Results obtained from the high-resolution method are plotted with bold lightblue letters, results from the MUSIC algorithm are indicated by the black characters in typewriter font. The thick dashed line at ∼3 s km^{-1} corresponds to the aliasing limit. The azimuth of the simulated event is shown by the red star.

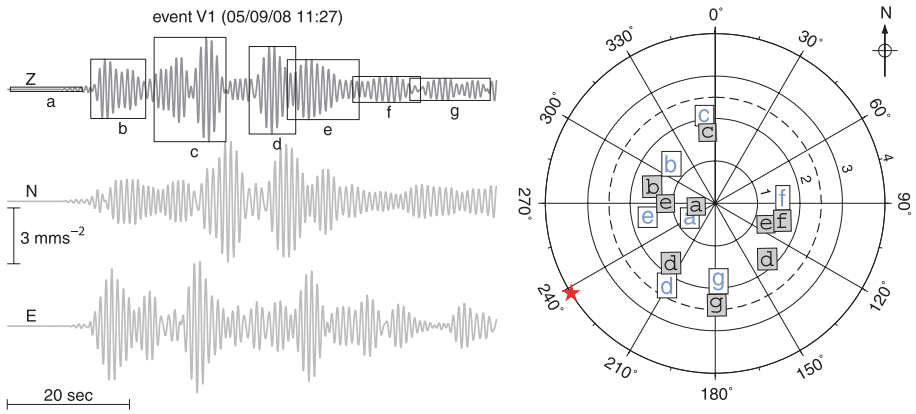

Figure 16. Results of *f–k* analysis at 1.1 Hz applied on recorded signals of the Vallorcine main shock (V1). See Fig. 15 for more explanation.

We applied the same processing to recorded signals of event N2 (Fig. 19). Both frequencies reveal arrivals from the epicentre direction for the first time window. Later time windows reveal surface waves arriving from all directions between the N–NW and SSW.

In summary, both simulated and recorded signals reveal Rayleigh surface waves originating at angles completely different from the epicentral direction. Such edge-generated surface waves have been reported from many numerical simulations (e.g. Bard & Bouchon 1980a; Kawase 1996; Olsen 2000), and there are a number of observations from recorded earthquakes (e.g. Field 1996; Joyner 2000; Frankel *et al.* 2001; Cornou *et al.* 2003; Hartzell *et al.* 2003). These edge-generated surfaces waves are likely the cause for amplification at frequencies above 1 Hz. The fact that arrivals from both basin sides can be observed (Figs 16 and 19) shows that these waves are not attenuating quickly enough within the embanked basin, at least not for weak ground motion at frequencies up to 2.5 Hz.

f-k spectra from observed ground motion are generally more complicated than those determined from synthetics and yield arrivals from more different directions. Once more, this difference can be traced back to the simple source description used in our simulations, where the incident wavefield was approximated by a plane *S*-wave. The lack of surface waves in the simulated incident wavefield may account for the reduced complexity of simulated *f-k* spectra compared with the observations.

The above analysis was done using Rayleigh waves only, hence we have not yet been able to identify edge-generated Love waves, which may also contribute significantly to the observed amplification on the horizontal components.

7 PEAK GROUND VELOCITIES

We computed peak ground velocities for all four simulated earthquakes and from all observations for the frequency range between 0 and 4 Hz. Peak velocities were normalized with the peak velocity at the reference station to estimate the amplification of the basin.

Fig. 20 (top panel) shows simulated site-to-reference peak velocities for the Vallorcine simulation. The highest values are encountered in a narrow-band at the valley centre, where peak velocities are four to six times higher than at the reference site. This belt of high amplification is caused by edge-generated surface waves arriving from both sides, which create positive interference near the valley centre. As can be seen in the snapshot at 4.20 s (Fig. 5), the two interfering surface waves combine to a V-shaped wave front with a central peak.

Outside the central band, the amplification ranges between 1 and 4. Amplification levels are highest in the central part of the model and vanish towards the boundaries. This distribution can be explained with the curvature of the valley boundary in the

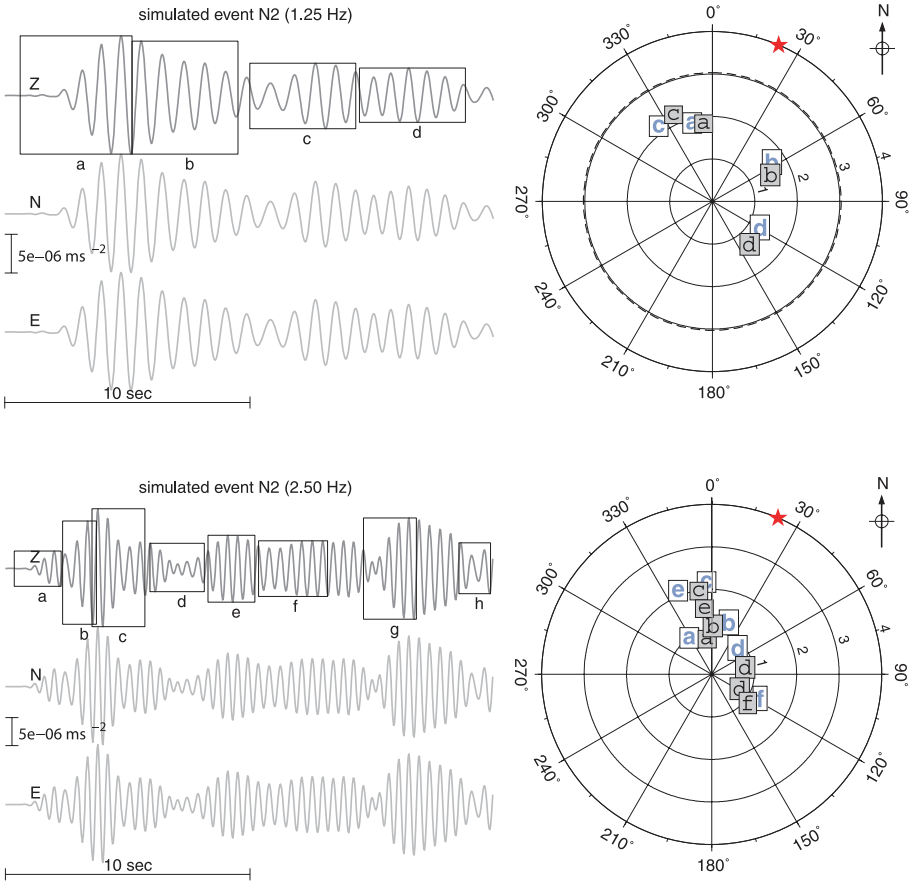

Figure 17. Results of *f*–*k* analysis at 1.25 (top) and 2.5 (bottom) Hz applied on synthetics of event N2. The aliasing limit for 2.5 Hz is outside the plotted range at 6 s km^{-1}.

north, which focuses edge-generated and reflected surface waves towards the model centre, and with the narrowing valley with at at longitude 7°22′. The vanishing peak velocities near the model border are probably just reflecting the vicinity to the absorbing boundaries.

Boxed numbers in Fig. 20 show the observed relative peak velocities. To allow comparison with the simulated values, observed signals were first low-pass filtered above 4 Hz. Observed normalized peak velocities are generally similar to the values derived from the simulation. Since the exact geometry of the basement is not known, one might speculate that the band of interference is actually located more to the south. This would explain the high observed peak velocity at station SIOTE and the extreme amplification observed at 3.5 Hz in spectral ratios (Fig. 8). Acceleration perpendicular to the valley axis (Fig. 4) shows a large-amplitude phase at the station SIOTE, just after the *S*-wave onset. We cannot verify this since no data is available for the station SIOSC, which is located right in the centre of the simulated interference zone. However, *f*-*k* analysis performed on recorded ground motion shows a first arrival similar to the simulation, which supports the interpretation of interfering edge-generated surface waves.

Peak velocities for the simulated Derborance main event D3 (Fig. 20 bottom panel) show a similar pattern in the central and northern part of the basin, though the amplification is generally lower. In the southern part of the basin, local maxima appear in the peak ground velocity pattern, which may also be related to interference effects between edge-generated surface waves.

Observed amplifications agree well with the simulation for the southern part of the basin; on the north side the observed amplifications are larger than the simulated values by up to 50 per cent.

Peak velocities show a more complicated distribution for events N2 and I3 (Fig. 21). The highest peak velocities are not concentrated in a central band, but distributed on spots located near the area of lowest shear wave velocities (Fig. 3). We presume that surface waves generated on the irregular northern margin of the basin (Fig. 18) exhibit a more complicated shape than the simpler wave trains observed from the Vallorcine simulation (Fig. 5). Therefore, the interference pattern is also getting more complex, which can be seen on the distribution of peak ground velocities (Fig. 21 top). Recorded peak velocities for the Vallorcine event are also exhibiting a stronger amplification and greater variability than from the other events.

Simulated peak velocities for the northern Italian event I3 yield a lower amplification of up to 5. The plane wave used to simulate event I3 is arriving from the southeast, but due to the steep angle of incidence, surface waves are generated both on the southern and the northern margin of the basin. Spots of intense shaking are more numerous on the south side, which reflects the lower shear wave velocities in that part of the velocity model.

Significant amplification of up to 4 also occurs in the tributary valley located north of the city centre. This amplification may be explained with surface waves generated on the east and west side of the trench, and to a lesser extent it can also be observed for the simulation of the Derborance and Vallorcine

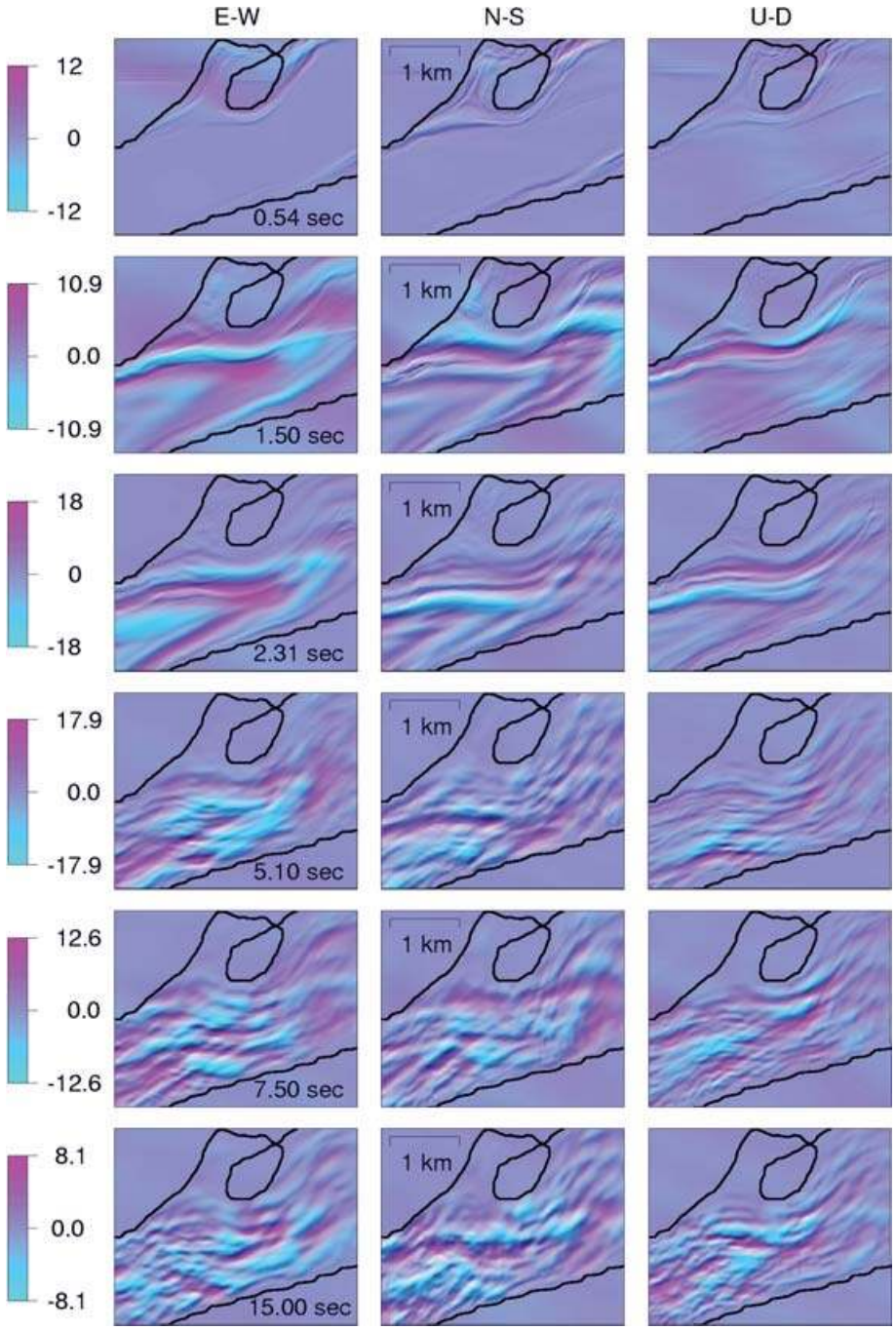

Figure 18. Snapshots of simulated wave propagation in the Sion basin after excitation with a plane wave arriving from the NNE, with input velocity from the Brugg event. Velocities are in 10^{-5} m s^{-1}.

main events (Fig. 20), but not for the Brugg event (Fig. 21 top panel). We cannot confirm this dependence on the direction of incidence from observations since no stations are available in this area.

Fig. 22 shows normalized peak ground velocities obtained from the simulation of the 1946 earthquake. The contour lines are plotted on a map of 1933, which reflects the approximate extent of the city at the time of the 1946 earthquake. Amplification levels of peak ground velocities are mostly lower than two in most parts of the town. This suggests that site effects did not contribute significantly to earthquake damage during the 1946 earthquake, at least not in the frequency range up to 4 Hz.

A reconstruction of the damage field (Stefan Fritsche Personal Communication 2007) supports this interpretation (red dots in Fig. 22). The damaged structures are quite uniformly distributed over the town, with no significant concentration of damage in specific areas. Additionally, sources are only describing light structural damage for most affected buildings, such as broken chimneys or cracked walls. A slight increase in the concentration of damaged structures can be observed towards the south and southwest

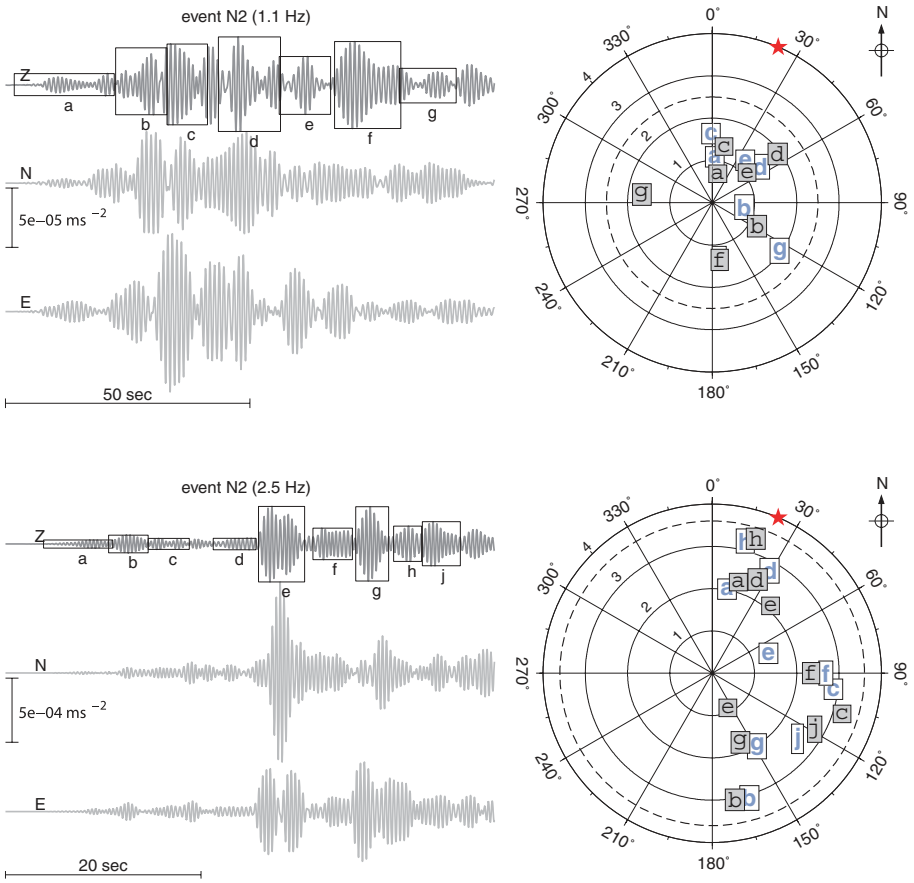

Figure 19. Results of f–k analysis at 1.10 (top) and 2.5 (bottom) Hz applied on records of event N2.

of the city, which is in agreement with the simulated peak ground velocities.

Certainly the validity of these results is limited due to the plane wave approximation and the uncertainties in the chosen source parameters. But, even for the other four simulated events (Figs 20 and 21), the amplification level of peak ground velocities remains mostly below 3 in the old town of Sion. This implies that the low simulated amplification in the old town of Sion reflects the relatively high shear wave velocities on the Sionne alluvial fan on which the town was built, rather than a source directivity effect.

The simulation of the 1946 event yields large amplification levels of up to 5 in the southwestern part of the basin, similarly to the events V1 and N2. However, no structures were located in that part of the basin at the time of the 1946 rupture.

8 SUMMARY AND CONCLUSIONS

We have analysed the seismic response of the Rhône valley at Sion from recorded weak motion signals and modelled the observations by numerical simulations of four selected events.

Site-to-reference Fourier spectral ratios of both horizontal components show a first peak at about 0.5–0.6 Hz, with an amplification level of up to 12 for some events. By analysing the motion perpendicular and parallel to the valley axis, we show that this peak is caused by the SH_{00} and SV_0 fundamental modes of 2-D resonance. The frequency of these modes remains constant regardless of the position along the basin, though we observe some variability with respect to the analysed event. This confirms results from previous numerical studies performed for the Rhône valley (Frischknecht & Wagner 2004; Frischknecht *et al.* 2005).

Fourier spectral ratios are also exhibiting significant amplification at frequencies above 1 Hz, especially at about 3 Hz at most sites and at 10 Hz for the site SIOAE. Amplification levels of up to 18 can be observed at these frequencies. We applied the high-resolution frequency-wavenumber technique and the multiple signal characterization method to both recorded and synthetic seismograms. Results from these spatial array techniques show that the wavefield is dominated by edge-generated surface waves arriving from directions specific to the analysed events.

For three simulated events, we observed constructive interference between surface waves generated at adjacent valley borders, which is reflected by a narrow-band of high peak ground velocities in the valley centre. This effect is considered as a possible explanation for the unusually high amplification observed at the station SIOTE in the valley centre, though our station spacing is not sufficient to confirm this assumption. Such central interference is only pronounced for plane waves arriving from the SW and NW; the interference pattern is getting more complicated for plane waves exciting the basin from the N–NE and SE. Peak ground velocities obtained from the simulation of the 1946 Sierre main shock yield no amplification in the old town of Sion, which suggests that site effects were of little importance for the damage reported after this historical earthquake.

The 3-D numerical simulations are able to explain the main characteristics of the observations, especially the SH_{00} and SV_0 fundamental mode 2-D resonance frequencies and the edge-generated surface waves. We conclude that shear wave velocities near the array centre are probably higher than the values used in our velocity

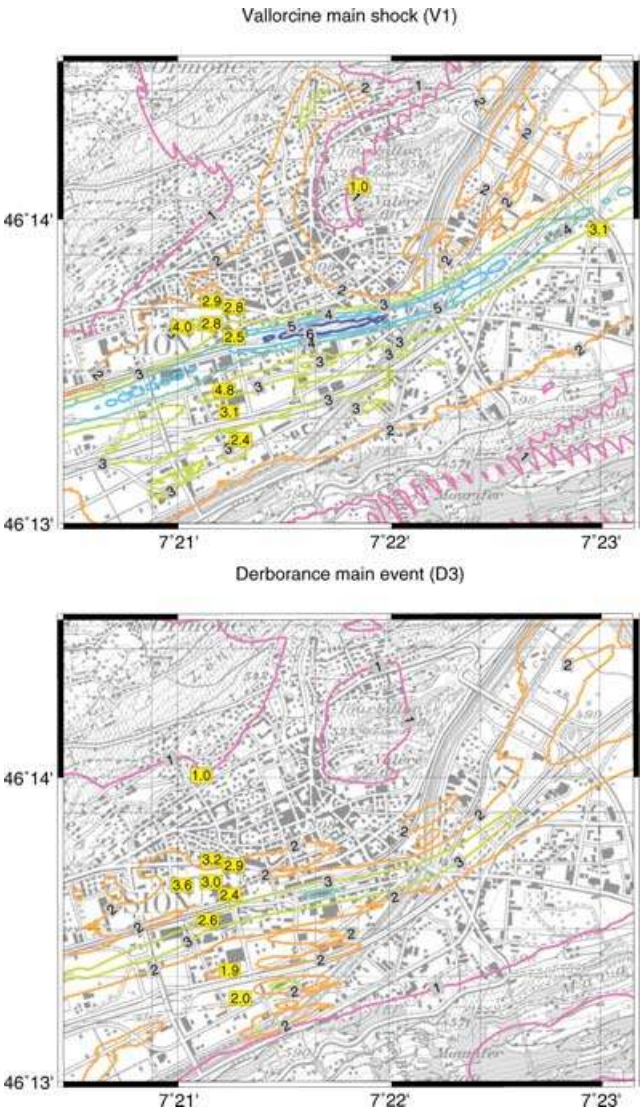

Figure 20. Simulated and observed peak ground velocities for the central part of the computational domain normalized by the peak ground velocity at the reference site. Numbers in grey rectangles and coloured contours represent the simulated normalized peak ground velocities; the numbers enclosed by yellow rectangles show the values observed at the available stations. The station on the north was used as a reference for both simulated and recorded peak ground velocities (PGA = 1.0). Reproduced by permission of Swisstopo (BA081013).

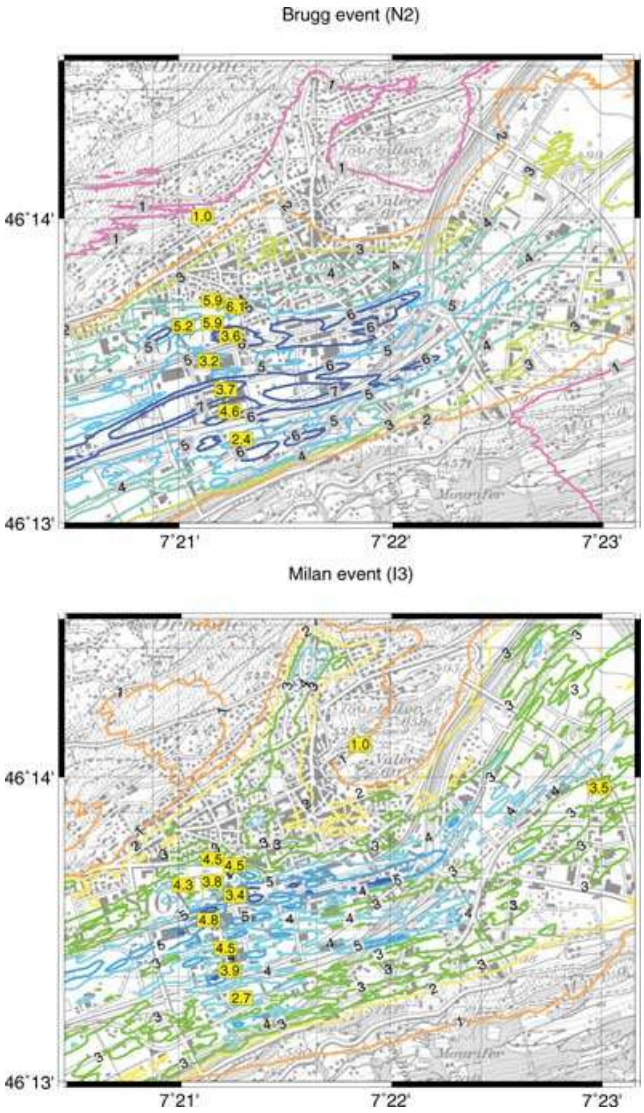

Figure 21. Like Fig. 20, but for events D3 and I3. Reproduced by permission of Swisstopo (BA081013).

model. This could mean that the higher-velocity, coarse material from the Sionne alluvial fan extends further to the south than we assumed. Higher shear wave velocities near the stations SIOAE and SIOTO would most likely improve the fit between observations and simulations at these sites (Fig. 11). For the stations SIOTE to SIOIS on the southern part of the basin, as well as for the site SIOO, the match between observations and simulations is generally quite good. Although our simulations have yielded amplification at frequencies above 1 Hz, they have not been able to match the frequencies of these peaks for the observed events (Figs 8–10). This shows that more attention should be directed to the details of the shallow structure, especially the depth and velocity contrast of the two uppermost layers down to depths of about 200 m.

Our results demonstrate that of 2-D and 3-D effects are important for the seismic response of the Sion basin, at least at frequencies up to 2.5 Hz. Peaks in observed Fourier spectral ratios suggest that edge-generated surface waves are also contributing to amplification at higher frequencies. Boreholes and ambient noise array measurements have revealed a shallow low-velocity layer of up to 10 m depth. We have not included this layer in our numerical simulations since our grid does not allow propagation of frequencies higher than 4 Hz. The amplification at ∼10 Hz observed at the stations SIOAE and SIOTO (Fig. 11) could be attributed to such a shallow layer. Although the frequency of the peak may be reproduced by 1-D analysis using

$$f = \frac{V_s}{4h}$$

(e.g. $V_s = 200$ m s^{-1} and $h = 5$ m), 1-D response alone is not able to cause an amplification level of up to 15 given the impedance contrast between the shallow layer and the deposits below. A combination of the basin edge effect with a shallow low-velocity layer or excitation of local surface waves inside the basin due to lateral heterogeneities could be possible explanations, but this should be verified by more detailed site investigations and higher-frequency numerical simulations.

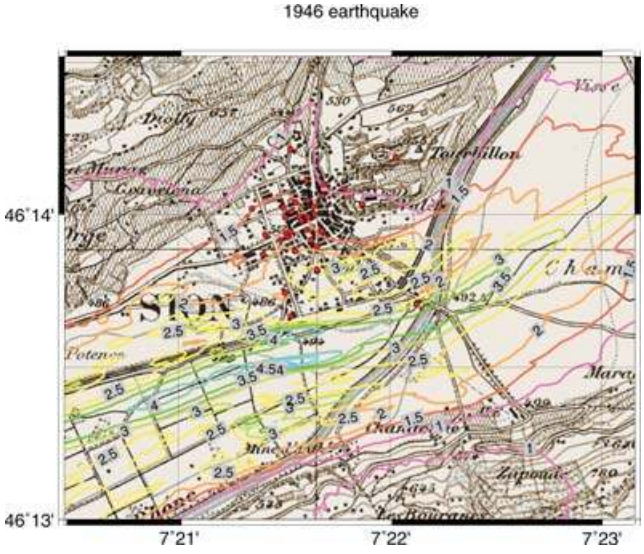

Figure 22. Normalized peak ground velocities obtained from the simulation of the 1946 Sierre main shock. The map dates back to 1933. Red dots show the location of buildings which suffered damage during the event (Stefan Fritsche, personal communication 2007).

We should keep in mind that the whole analysis presented in this text was focusing on weak ground motion, and the studied sites may respond to a future *M* 6 event in a different way. Some indications of non-linear soil behaviour were observed in the Rhône valley after the 1946 earthquake (Fritsche *et al.* 2006). Although non-linear effects are unlikely to affect the deep resonance of the basin, the response of the shallow sandy layer may be modified significantly. This issue is currently being addressed with a fully non-linear 1-D model of wave propagation (Bonilla *et al.* 2005).

ACKNOWLEDGMENTS

We wish to thank the town of Sion and various individuals who supported us by operating seismic stations on their premises. Thomas Stalder, Beat Rinderknecht, Peter Zweifel and other people from the electronics laboratory helped to implement the temporary array. Cécile Cornou assisted in site selection. Valentin Gischig was in charge of station maintenance. The routines for computation of Capon and MUSIC spectra were implemented by Matthias Ohrnberger. The 3-D FD simulations were run on the Babieca cluster at San Diego State University, with support from Yifeng Cui and James Otto. We wish to thank two anonymous reviewers for their valuable comments which helped to improve the manuscript. This research is part of the Interreg project SISMOVALP and the project SHAKE-VAL, funded by the Swiss National Science Foundation (No. 200021-101920 and 200020-109177).

REFERENCES

Ambraseys, N., Smit, P., Sigbjörnsson, R., Suhadolc, P. & Margaris, B., 2001. Internet-Site for European Strong-Motion Data, available at http://www.isesd.cv.ic.ac.uk, EVR1-CT-1999-40008, European Commission, Directorate-General XII, Environmental and Climate Programme, Bruxelles, Belgium.

Baer, M. *et al*., 2005. Earthquakes in Switzerland and surrounding regions during 2004, *Eclogae geol. Helv.,* **98,** 407–418.

Bard, P.-Y. & Bouchon, M., 1980a. The seismic response of sediment-filled valleys. Part 1: the case of incident SH waves, *Bull. seism. Soc. Am.,* **70**(4), 1263–1286.

Bard, P.-Y. & Bouchon, M., 1980b. The seismic response of sediment-filled valleys. Part 2: the case of incident P and SV waves, *Bull. seism. Soc. Am.,* **70**(5), 1921–1941.

Bard, P.-Y. & Bouchon, M., 1985. The two-dimensional resonance of sediment-filled valleys, *Bull. seism. Soc. Am.,* **75**(2), 519–541.

Baumann, M., 1994. Three-dimensional seismic image of the Alpine crustal structure, *PhD thesis*, ETH Zürich.

Besson, O., Marchant, R., Pugin, A. & Rouiller, J.-D., 1993. Campagne de sismique-réflexion dans la vallée du Rhône entre Sion et St. Maurice: perspectives d'exploitation géothermique des dépôts torrentiels sous-glaciaires, *Bull. du Centre d'hydrogéologie de l'Université de Neuchâtel,* **12,** 39–58.

Bonilla, L.F., Archuleta, R.J. & Lavallee, D., 2005. Hysteretic and dilatant behavior of cohesionless soils and their effects on nonlinear site response: field data observations and modeling, *Bull. seism. Soc. Am.,* **95**(6), 2373–2395.

Capon, J., 1969. High-resolution frequency-wavenumber spectrum analysis, *Proc. IEEE,* **57**(8), 1408–1419.

Cerjan, C., Kosloff, D. & Reshef, M., 1985. A nonreflecting boundary condition for discrete acoustic and elastic wave equations, *Geophysics,* **50,** 705–708.

Cornou, C., Bard, P.-Y. & Dietrich, M., 2003. Contribution of dense array analysis to the identification and quantification of basin-edge-induced waves. Part II: application to Grenoble basin (French Alps), *Bull. seism. Soc. Am.,* **93,** 2624–2648.

Deichmann, N. *et al.*, 2007. Earthquakes in Switzerland and surrounding regions during 2005, *Eclogae geol. Helv.,* **99,** 443–452.

Fäh, D. *et al.*, 2003. Earthquake catalogue Of Switzerland (ECOS) And the related macroseismic database, *Eclogae geol. Helv.,* **96,** 219–236.

Field, E.H., 1996. Spectral amplification in a sediment-filled valley exhibiting clear basin-edge-induced waves, *Bull. seism. Soc. Am.,* **86,** 991–1005.

Frankel, A. & Vidale, J., 1992. A three-dimensional simulation of seismic waves in the Santa Clara Valley, California, from a Loma Prieta aftershock, *Bull. seism. Soc. Am.,* **82,** 2045–2074.

Frankel, A., Carver, D., Cranswick, E., Bice, T., Sell, R. & Hanson, S. 2001. Observations of basin ground motion from a dense seismic array in San Jose, California, *Bull. seism. Soc. Am.,* **91,** 1–12.

Frischknecht, C. & Wagner, J.-J., 2004. Seismic soil effect in an embanked deep Alpine Valley; a numerical investigation of two-dimensional resonance, *Bull. seism. Soc. Am.,* **94,** 171–186.

Frischknecht, C., Rosset, P. & Wagner, J.-J., 2005. Toward seismic microzonation – 2-D modeling and ambient seismic noise measurements: the case of an embanked, deep Alpine Valley, *Earthq. Spectra,* **21**(3), 635–651.

Fritsche, S., Fäh, D., Gisler, M. & Giardini, D., 2006. Reconstructing the damage field of the 1855 earthquake in Switzerland: historical investigations on a well-docomented event. *Geophys. J. Int.,* **166**(2), 719–731.

Hartzell, S., Carver, D., Williams, R.A., Harmsen, S. & Zerva, A., 2003. Site response, shallow Shear-wave velocity, and wave propagation at the San Jose, California, Dense Seismic Array, *Bull. seism. Soc. Am.,* **93**(1), 443–464.

Hough, S.E., Friberg, P.A., Busby, R., Field, E.F., Jacob, K.H. & Borcherdt, R.D., 1990. Sediment-induced amplifcation and the collapse of the Nimitz Freeway, *Nature,* **344,** 853–855.

Joyner, W.B., 2000. Strong motion from surface waves in deep sedimentary basins, *Bull. seism. Soc. Am.,* **90**(6B), S95–S112.

Kawase, H., 1996. The cause of the damage belt in Kobe: "The basin-edge effect," constructive interference of the direct S-wave with the basin-induced diffracted/Rayleigh waves, *Seism. Res. Lett.,* **67**(5), 25–34.

Kind, F., Fäh, D. & Giardini, D., 2005. Array measurements of S-wave velocities from ambient vibrations, *Geophys. J. Int.,* **160,** 114–126.

Konno, K. & Ohmachi, T., 1998. Ground-motion characteristics estimated from spectral ratio between horizontal and vertical components of microtremor, *Bull. seism. Soc. Am.,* **88**(1), 228–241.

Marcos, S. 1998. *Les méthodes à haute résolution: traitement d'antenne et analyse spectrale*. Edition Hermès, Paris.

Maurer, H. 1993. Seismotectonics and upper crustal structure in the western Swiss Alps, *PhD thesis*, ETH Zürich.

Ohrnberger, M. *et al.*, 2004. *User manual for software package CAP — a continuous array processing toolkit for ambient vibration array analysis*, SESAME deliverable D18.06, SESAME EVG1-CT-2000-00026 project, available at http://sesame-fp5.obs.ujf-grenoble.fr.

Olsen, K.B. 1994. Simulation of three-dimensional wave propagation in the Salt Lake Basin, *PhD thesis*, University of Utah, Salt Lake City, Utah.

Olsen, K.B., 2000. Site amplification in the Los Angeles basin from 3D modeling of ground motion, *Bull. seism. Soc. Am.,* **90,** S77–S94.

Olsen, K.B. *et al.*, 2006. TeraShake: strong shaking in Los Angeles expected from southern San Andreas earthquake, *Seism. Res. Lett.,* **77,** 281–282.

Paolucci, R., 1999. Shear resonance frequencies of alluvial valleys by Rayleigh's method, *Earthq. Spectra,* **15**(3), 503–521.

Pfiffner, O.A., Heitzmann, S., Mueller, S. & Steck, A., 1997. Incision and backfilling of Alpine valleys: pliocene, pleistocene and Holocene processes, in *Deep Structure of the Swiss Alps — Results of NRP 20*, pp. 265–276, Birkhäuser, Basel.

Rosselli, A. 2001, Modélisation gravimétrique bi- et tridimensionelle du substratum rocheux des vallées alpines, *PhD thesis*, Université de Lausanne.

Roten, D. & Fäh, D., 2007. A combined inversion of Rayleigh wave dispersion and 2-D resonance frequencies, *Geophys. J. Int.,* **168,** 1261–1275.

Roten, D., Cornou, C., Fäh, D. & Giardini, D., 2006. Two-dimensional resonances in Alpine valleys identified from ambient vibration wavefields, *Geophys. J. Int.,* **165,** 889–905.

Schmidt, R., 1986a. Multiple emitter location and signal parameter estimation, *IEEE Trans. Ant. Prop,* **34**(3), 276–280.

Schmidt, R., 1986b. Multiple source df signal processing: an experimental system, *IEEE Trans. Ant. Prop,* **34**(3), 281–290.

Steimen, S., Fäh, D., Kind, F., Schmid, C. & Giardini, D., 2003. Identifying 2D resonance in microtremor wave fields, *Bull. seism. Soc. Am.,* **93**(2), 583–599.

Wanner, E., 1955. Die Lage der Erdbebenherde im Mittelwallis, *Eclogae geol. Helv.,* **48**(2), 245–255.

Wathelet, M. D., Jongmans & Ohrnberger, M., 2004. Surface wave inversion using a direct search algorithm and its application to ambient vibration measurements, *Near Surf. Geophys.,* **2,** 211–221.

Wax, M. & Kailath, T., 1985. Detection of signals by information theoretic criteria, *IEEE Transactions on ASSP,* **33**(2), 387–392.

Zerva, A. & Zhang, O., 1996. Estimation of signal characteristics in seismic ground motion, *Prob. Eng. Mech.,* **11,** 229–242.

SUPPLEMENTARY MATERIAL

The following supplementary material is available for this article:

Movie S1. An animation of the 1946 simulation (avi format).
Movie S2. A simulation of event V1 (avi format).

This material is available as part of the online article from: http://www.blackwell-synergy.com/doi/abs/10.1111/j.1365-246X.2008.03774.x (this link will be take you to the article abstract).

Pleate note: Blackwell Publishing is not responsible for the content or functionality of any supplementary materials supplied by the authors. Any queries (other than missing material) should be directed to the corresponding author for the article.